Yoon, J.-S., Zang, A., Stephansson, O. (2014): Numerical investigation on optimized stimulation of intact and naturally fractured deep geothermal reservoirs using hydro-mechanical coupled discrete particles joints model. - *Geothermics*, *52*, p. 165-184.

DOI: http://doi.org/10.1016/j.geothermics.2014.01.009

Geothermics 52 (2014) 165-184
doi: 10.1016/j.geothermics.2014.01.009

Numerical investigation on optimized stimulation of intact and naturally fractured deep geothermal reservoirs using hydro-mechanical coupled discrete particles joints model

Jeoung Seok Yoon*, Arno Zang, Ove Stephansson

Section 2.6 Seismic Hazard and Stress Field, Helmholtz Centre Potsdam, GFZ German Research Centre for Geosciences, Telegrafenberg, 14473 Potsdam, Germany

ARTICLE INFO

Article history:
Received 16 November 2012
Received in revised form
10 December 2013
Accepted 21 January 2014
Available online 14 February 2014

Keywords:
Reservoir stimulation
Fluid injection
Induced seismicity
Discrete particle joints model
Particle Flow Code
Soft stimulation

ABSTRACT

This numerical study investigates hydraulic fracturing and induced seismicity in intact and fractured reservoirs under anisotropic in situ stress using hydro-mechanical coupled discrete particles joints model. A 2 km × 2 km reservoir model with granitic rock and joints properties is constructed. Various injection scenarios are tested which involve continuous and cyclic styles of pressure controlled and flow rate controlled injections. Results are compared which include: spatial and temporal evolution of induced seismic events in relation with fluid pressure distribution, moment magnitudes of the induced events, occurrence of post-shut-in large magnitude events, etc. Several field observations on induced seismicity phenomena are simulated which include creation of new fractures, re-activation of the pre-existing joints, post-shut-in seismicity and large magnitude event with non-double-couple source, Kaiser phenomenon, moment magnitude vs. frequency distribution of the induced events following the Gutenberg-Richter law, etc. Cyclic injection results in larger volume of injected fluid but less number of total events and larger magnitude events; hence less seismic energy radiated by the induced events, slower relaxation of the fluid pressure after shut-in, longer and thinner propagated fractures with larger fluid saturated area. The major conclusions of this study are that the presented modeling is capable of simulating induced seismicity phenomena in Enhanced Geothermal System and fluid injection in fractured reservoirs in cyclic way has potential in mitigating the effects of larger magnitude induced events.

1. Introduction

Developing an Enhanced Geothermal System (EGS) in deep reservoir requires creation of highly permeable heat exchanger which is usually achieved by fluid injection that results in combination of propagation of new fractures (hydro-fracturing) and induced slip on pre-existing fractures (hydro-shearing) referred to as Mixed-Mechanism stimulation (MMS, *McClure and Horne*, 2013). Fluid injection causes stress field changes and re-activation of the pre-existing joints and slip of nearby faults which consequently can result in larger magnitude events, e.g. local magnitude of 3.4 event in Basel EGS operation (*Kraft et al.*, 2009). These largest events tend to occur on the fringes, outside the "main cloud" of seismicity and are often observed after well shut-in, making them difficult to control (*Mukuhira et al.*, 2013). The need for developing a solid understanding of the processes underlying the occurrence of post-shut-in seismicity has become an important issue world-wide (*Majer et al.*, 2007). Such phenomena have led to development of numerical tools that are able to simulate fluid injection in rock mass and interactions between injected fluid, rock mass and joints, creation of new fractures and re-activation of pre-existing joints. Appropriate measure for mitigating the effects of large magnitude events and optimizing EGS can be established after reliability of the numerical tools is validated.

In this context, this paper introduces hydro-mechanical coupled discrete particles joints model applied to simulation of hydraulic fracturing and induced seismicity in synthetic reservoirs. Particle Flow Code 2D (*PFC^{2D}*) (*Itasca*, 2008) with additionally implemented fluid flow algorithm and seismicity computation algorithm is used. Similar studies have been conducted using *PFC^{2D}* by *Hazzard et al.* (2002), *Al-Busaidi et al.* (2005), *Yoon and Jeon* (2009), *Zhao and Young* (2011), *Shimizu et al.* (2011, but not using PFC^{2D}). *Hazzard et al.* (2002) simulated a fluid injection test conducted in granitic rock at Soultz-sous-Forêts, France. *Al-Busaidi et al.* (2005) investigated the initiation and propagation of hydrofractures and the resulting seismic output, by comparing the results from lab-scale model simulation with the laboratory experiments. *Yoon and Jeon* (2009) performed numerical modeling of fracturing processes in rocks induced by blast loading. *Zhao and Young* (2011) investigated interaction between hydraulic fracture and single natural joint. *Shimizu et al.* (2011) conducted a series of simulations for hydraulic fracturing in competent rock and investigated the influence of the fluid viscosity and the particle size distribution.

This paper presents various fluid injection schemes tested in two different reservoir models – intact and naturally fractured – that have granitic properties. Results are compared which include: (1) spatial and temporal evolution of the induced seismic events in relation with fluid pressure distribu-

* Corresponding author. Tel.: +49 331 288 1716; fax: +49 331 288 1127.
E-mail addresses: jsyoon@gfz-potsdam.de, yoon_gfz@hotmail.com (J.S. Yoon), arno.zang@gfz-potsdam.de (A. Zang), ove@gfz-potsdam.de (O. Stephansson)

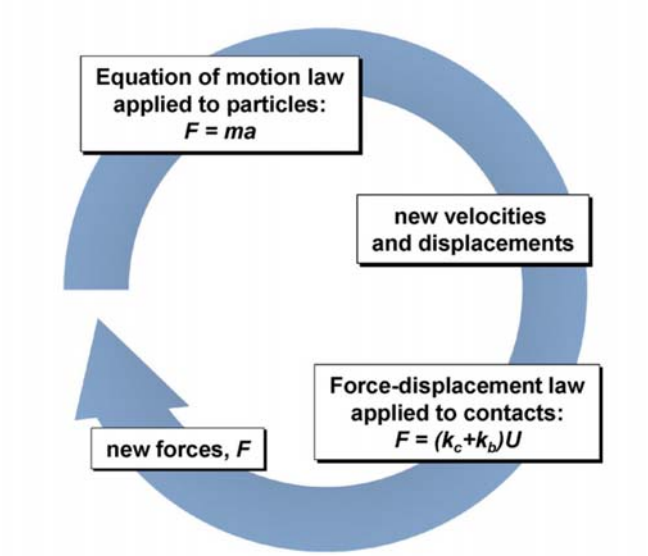

Figure 2. Calculation cycle in *PFC²ᴰ* (m: particle mass, a: acceleration, k_c: contact stiffness, k_b: bond stiffness, U: particle overlap).

tion, (2) moment magnitudes of the induced events, (3) occurrence of post-shut-in large magnitude events, etc. Main objectives of this numerical study are (i) to examine if the presented numerical method is capable of reproducing the typically observed induced seismicity phenomena in EGS and (ii) to test two injection schemes – continuous and cyclic injections – and to see how the induced event clouds differ in terms of number of induced events, magnitude distribution, post-shut-in seismicity, occurrence of induced events in relation to fluid pressure distribution in intact and fractured reservoirs, etc. and finally (iii) to provide insights for how one can make use of soft stimulation to mitigate the effects of large magnitude induced seismicity and at the same time optimize the reservoir.

2. Methodology

2.1. Particle Flow Code 2D (PFC²ᴰ)

PFC²ᴰ is a two-dimensional distinct element geomechanical modeling software (*Itasca*, 2008). The material simulated, in this case a reservoir rock mass, is modeled as an aggregate of circular particles bonded at their contacting points with finite thickness of cementing around the contact with the Mohr–Coulomb strength parameters (Table 1, *Itasca*, 2012 – enhanced parallel bond model). Under an applied load, the bonds can break in Mode I (tensile) or Mode II (shear). The calculation cycle in *PFC²ᴰ* is a time stepping algorithm that requires repeated application of the law of motion applied to each particle and a linear force displacement law applied to each contact (Fig. 1). For more detail, we refer to *Potyondy and Cundall* (2004).

2.2. Fluid flow algorithm

Flow of viscous fluid in bonded particle assembly and fluid pressure and volume driven breakages of bonds in Mode I and Mode II are simulated. Original concept of fluid flow algorithm is proposed by Cundall (unpublished technical note, 2000), which was later modified by *Hazzard et al.* (2002).

Fluid flow is simulated by assuming that each particle bonded contact is a flow channel (Fig. 2, blue lines) and these channels connect up pore spaces (Fig. 2, polygons) that can store pressure. Pressure driven flow of viscous fluid between

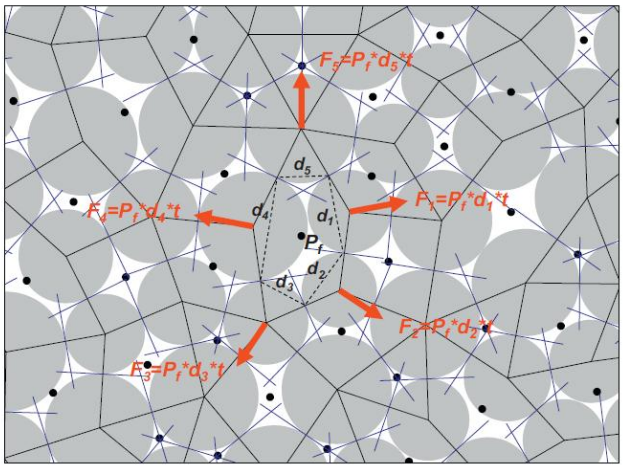

Figure 1. Pore network model. Flow channels (blue lines at the particle contacts) are connecting two neighboring pore spaces bounded by polygons. Black dots at the polygon centers are virtual pores where pressure (P_f) is stored. Red arrows are resultant forces applied to the particles surrounding the pore space due to the pore fluid pressure P_f. (For interpretation of the references to color in this figure legend, the reader is referred to the web version of this article.)

the two pore spaces is governed by Cubic law (Table 1) assuming that the flow is laminar between two smooth parallel plates.

$$q = \frac{e^3 \Delta P_f}{12\eta L} \tag{1}$$

where, e is hydraulic aperture, ΔP_f is fluid pressure difference between the two neighboring pores, L is flow channel length, η is fluid dynamic viscosity (Table 1).

Hydraulic aperture e, of the flow channel at a particle contact (Fig. 2, blue lines) changes as a function of normal stress, σ_n. We used experimentally derived e vs. σ_n n relation from *Hökmark et al.* (2010).

$$e = e_{\text{inf}} + (e_0 - e_{\text{inf}})\exp(-0.15\sigma_n) \tag{2}$$

where, e_{inf} is hydraulic aperture at infinite normal stress, e_0 is hydraulic aperture at zero normal stress, σ_n is effective normal stress at the particle contact.

Fluid pressure increase per time step in a pore space (ΔP_f, Fig. 2) is computed from the fluid bulk modulus (K_f), volume of pore space (V_d), sum of flow volume (q, entering and leaving the pore space) and volume change of pore space (ΔV_d) due to mechanical loading, which is neglected in this study due to its minor effect. The equation used is shown below.

$$\Delta P_f = \frac{K_f}{V_d}\left(\sum q\Delta t - \Delta V_d\right) \tag{3}$$

The fluid exerts pressure on the surrounding particles causing deformations. This force term (F) is a production of fluid pressure (P_f), the length d (Fig. 2) and unit thickness (1 m) in out-of-plane direction. The resulting force term (F) is then applied to the particles from which law of motion computes the particle velocity and displacement which subsequently changes the stress states at the surrounding contacts which in turn changes the hydraulic aperture and thereby flow field.

Using the bonded particle assembly and the fluid flow algorithm, we constructed a 2D reservoir model which is assumed to be naturally fractured and located at deep depth (Fig. 3a) and subjected to differential in situ stresses.

Table 1
Model parameters used to generate synthetic granitic intact and naturally fractured reservoirs.

Property	Value (unit)	Reference/remarks
Intact rock		
Density	2600 kg/m^3	
UCS	115 ± 15 MPa	*Valley and Evans* (2006)
Tensile strength, T_0	11.5 ± 1.5 MPa	10% of UCS
Cohesion, c	30 ± 5 MPa	
Friction angle, ϕ	52°	Aue granite (*Yoon et al.*, 2012)
Friction coefficient, μ[a]	0.9	*Cornet et al.* (2007)
Young's modulus, E	60 GPa	*Valley and Evans* (2006)
Poisson's ratio, ν	0.25	*Evans et al.* (1998)
Discrete joints		
Normal stiffness, k_n	200 GPa/m	
Shear stiffness, k_s	50 GPa/m	
Friction coefficient, μ[a]	0.9	*Cornet et al.* (2007)
Friction angle, ϕ_f	30°	
Dilation angle, φ_f	3°	
Tensile strength, $T_{0,f}$	0 MPa	
Cohesion, c_f	0.5 MPa	
Joint set length and orientation		
No. joint set/per set	3/10	
Joint set half-length	Set1: 150–200 m, Set2: 0–150 m, Set3: 200–300 m	
Joint set strike direction	Set1: S10°–30°E (N170°E, *Baria et al.*, 1999) Set2: N10°–30°E (N10°E, *Baria et al.*, 1999) Set3: S40°–60°E (N132°E, *Gentier et al.*, 2010)	
In situ stresses		
S_H	75 MPa	At 4 km depth, *Rummel and Baumgartner* (1991)
S_h	60 MPa	At 4 km depth, *Rummel and Baumgartner* (1991)
Seismic		
Quality factor, Q	140	*Michelet and Toksöz* (2005)
S-wave velocity	3500 m/s	*Cuenot et al.* (2008)
Hydraulic		
Permeability, k	10^{-12} m^2	
Flow equation	Cubic law	$q = \left(e^3 \Delta P_f\right)/(12\eta L)$
Fluid viscosity, η	1e−3 Pa s	
e vs. σ_n relation	$e = e_{\text{inf}} + (e_0 - e_{\text{inf}})\exp(-0.15\sigma_n)$	*Hökmark et al.* (2010)
Fracture aperture, e_0	650 μm	Flow channel aperture at zero σ_n
Fracture aperture, e_{inf}	50 μm	Flow channel aperture at ∞ σ_n
Fluid pressure increase	$\Delta P_f = \left(K_f/V_d\right)\left(\sum Q\Delta t - \Delta V_d\right)$	*Hazzard et al.* (2002)
Fluid bulk modulus, K_f	2.2 GPa	
Formation pressure, P_{ini}	0 MPa	
Fracture breakdown pressure (FBP) estimates		
FBP equation	$P^{HF} - P_{\text{ini}} = (3S_h - S_H + T_0)/b$	*Zang and Stephansson* (2010)
Lower and upper estimates	80, 85 MPa	
Denominator, b	1.44	

[a] Friction coefficient is applied for frictional sliding at the contacts after breakages of parallel and smooth joint bonds.

2.3. Representation of in situ discrete pre-existing joints

Classical way of representing joints in assemblies of bonded particles is to debond contacts along a line or plane and to assign low strength and stiffness microproperties (*Kulatilake et al.*, 2001; *Park et al.*, 2004; *Zhao and Young*, 2011). This way of representing joints is problematic due to the inherent roughness of the surface, i.e. very low friction assigned to the contacts does not lead to realistic sliding due to the roughness or asperity induced by the circular particles.

We used, in this study, smooth joint contact model (*Mars Ivars et al.*, 2008) to mimic the in situ joint fabric (Fig. 3a). By using smooth joint contact model some of limitations of the earlier work are overcome. By bounding angular blocks of bonded particle with smooth rather than bumpy boundaries, it is possible to more accurately model the role of block angularity and interlocking on rock mass strength and brittleness (*Mars Ivars*, 2010).

For the in situ joint fabric, three sets of joints are stochastically generated from the uniform distributions for the orientation and the length (Table 1). Three sets of joints are generated of which major orientations are taken from *Baria et al.* (1999) and *Gentier et al.* (2010). Length scales and numbers of joints per set are arbitrarily determined. The generated joint fabric is then overlaid on to the bonded particle assembly. Those particle contacts which were assigned with parallel bonds and located along the joint fabric are switched to smooth joint contacts (Fig. 3b) and assigned with mechanical properties that are listed in Table 1.

2.4. Seismicity computation

Each bond breakage in the bonded particle assembly is assumed to be a fracture process associated with seismic energy radiation. *PFC^{2D}* runs in dynamic mode with low levels of numerical damping where a realistic level of energy attenuation in rock is simulated. For simulating the realistic level of energy attenuation we use the seismic quality factor $Q = 140$ (*Michelet and Toksöz*, 2005) which is then converted to a local damping coefficient ($\alpha = \pi/2Q$) assigned to the particles.

Upon a bond breakage by Mode I or Mode II, part of accumulated strain energy at the broken bond is released to the surrounding in a form of seismic wave. A numerical technique for calculating the seismic source information in *PFC^{2D}* has

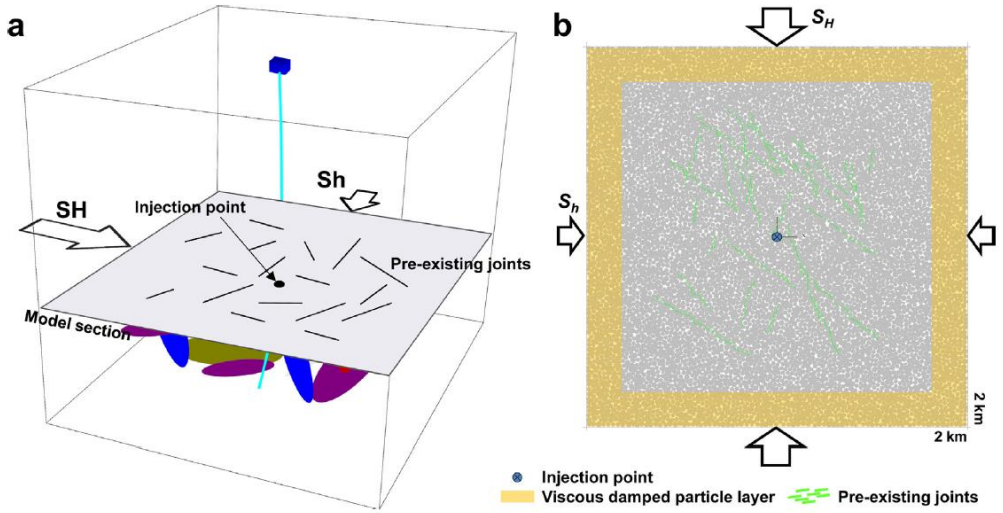

Figure 3. (a) 3D schematic view of fluid injection in naturally fractured reservoir. (b) Reservoir model (2 km × 2 km in size) with embedded discrete pre-existing joints and viscous damped layer near boundaries and subjected to differential in situ stresses (S_H = 75 MPa, S_h = 60 MPa).

been proposed by *Hazzard and Young* (2002, 2004) and used in *Hazzard et al.* (2002), *Al-Busaidi et al.* (2005), *Zhao and Young* (2011), *Yoon et al.* (2012, 2013) and *Zang et al.* (2013).

In this study, a link was made in the algorithm to compute seismic source parameters of the Mode I (tensile) and Mode II (shear) failures at the pre-existing joints, i.e. breakages of smooth joint bonds. Currently, seismic source parameters are obtained only for bond breakage by Mode I (Fig. 4a) and Mode II (Fig. 4b) and not for the subsequent sliding after shear bond breakage, i.e. silent frictional slip. Ongoing research aims at computing the seismic moment and moment magnitude of the frictional sliding event at the smooth joint contact that is broken by shear. This is necessary as energy can be released also by slip (*Marone*, 1998). Large number of relatively lower magnitude events caused by slipping can result in more exponential distribution of the magnitude-frequency relation similar to the Gutenberg-Richter law.

For each bond breakage, the moment tensor is calculated for each time step over the duration of the event. The duration of an event is determined by assuming that a shear fracture propagates at half the shear wave velocity (3500 m/s in Table 1) of the rock to the edge of the source area (one particle diameter). If another crack forms adjacent to the active crack such that the source area overlap within the duration of the event, then the cracks are considered part of the same event, i.e. two cracks but one event. This approach is thought to be a realistic assumption as it is known that most seismic events in the field are made up of many smaller scale ruptures and shearing of asperities (*Scholz*, 1990) and that fractures generally grow at some finite velocity (*Madariaga*, 1976). This is the reason why the total number of induced events differs from the total number of cracks (bond breakages), i.e. sum of Mode I and Mode II bond breakages of rock and joint (Table 2).

Ongoing research aims at simulating temporal and spatial change in S-wave velocity for the seismicity computation algorithm. This approach may be necessary as the S-wave velocity of an undisturbed geothermal reservoir (before stimulation) can change significantly as the fluid is injected and induces fractures which serve as barriers for S-wave propagation.

The moment tensor of each event is then decomposed into isotropic and deviatoric parts and their respective percentage is quantified as:

$$R = \frac{tr(M) \times 100}{\left(|tr(M)| + \sum|m_i^*|\right)} \quad (4)$$

where, $tr(M)$ is the moment tensor trace and m_i^* are the deviatoric eigenvalues. The ratio R varies from 100 (explosion) to −100 (implosion), and $R = 0$ indicates a pure shear failure mechanism. In this study, events are considered 'tensile' if the R value is greater than 30%, 'implosion' if it is smaller than −30% and 'shear' for a R value ranging from −30% to +30% (*Feignier and Young*, 1992). In addition to the source mechanisms, seismic radiated energy Es of the induced events is computed using the equation by *Gutenberg and Richter* (1956) as a function of moment magnitude M_w:

$$\log(Es) = 4.8 + 1.5M_w \quad (5)$$

3. Modeling procedure

3.1. Model description and parameters

The reservoir model is 2 km × 2 km in size (Fig. 3b). Diameters of particles to pack the given space are in range between 20 and 30 m, resulting in ca. 7500 particles. The diameter range chosen is comparable to that used in a similar study by *Hazzard et al.* (2002, average particle diameter = 19.7 m) and the Block-Spring model by *Baisch et al.* (2010, fracture zone consists of individual blocks of 20 m side length). The model contains three sets of joints with their orientation distribution, length scale, strength and stiffness properties defined in Table 1.

There are no specific hydraulic properties assigned to the smooth joint contacts, i.e. pre-existing joints. However, relatively large hydraulic apertures (e_0 in Table 1) are assigned for those contacts which are broken while applying the initial in situ stresses. Such pre-damaged and isolated cracks serve as non-persistent pre-existing joints with high permeability. After model is constructed and discrete joints are embedded, the model is com-pressed to achieve internal principal stresses $\sigma_1 = \sigma_{yy} = 75$ MPa and $\sigma_2 = \sigma_{xx} = 60$ MPa as in situ stresses. The model is assumed to be at 4 km depth (z), using the stress-depth relation at Soultz from *Rummel and Baumgartner* (1991), which are equations 1b and 1c in *Cornet et al.* (2007).

Along and near the boundaries, 150 m thick region (shaded region, Fig. 3b) is assigned with high viscous damping properties in both normal and shear directions to simulate energy absorption and minimize wave reflection. This is to

Table 2
Summary of the results of ten fluid injection scenarios.

Pressure controlled simulations Intact reservoir		Fluid pressure distribution at indicated time (red: P_f = 75 MPa, blue: P_f = 0.1 MPa)
Monotonic injection		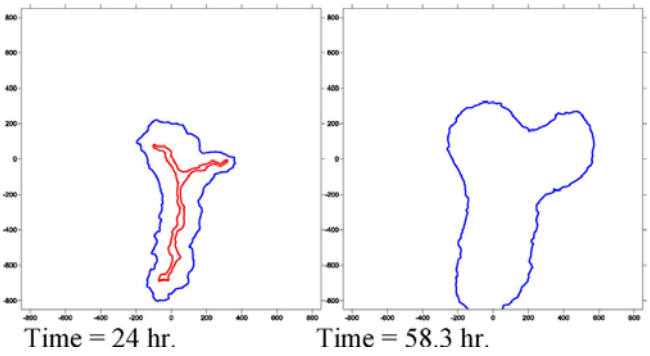
Total no. of events	194	
No. rock tensile/shear cracks	189/9	
No. joint tensile/shear cracks	–/–	
No. pre-/post-shut-in events	135/59	
% of pre-/post-shut-in events	70/30	
Avg. M_w of pre-/post-events	−0.03/−0.27	
1st largest M_w event[a]	0.55, +9% (S), post	
2nd largest M_w event[a]	0.52, −24% (S), pre	
3rd largest M_w event[a]	0.46, −45% (I), pre	
$M_w M_w$ range	−0.75 to 0.55	
Total Es	13 MJ	
Average M_w	−0.10	
Std. dev. M_w	0.27	
Cyclic 5 MPa residual injection		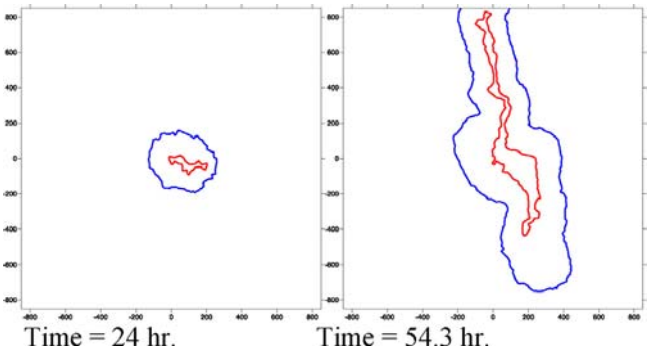
Total no. of events	357	
No. rock tensile/shear cracks	378/15	
No. joint tensile/shear cracks	–/–	
No. pre-/post-shut-in events	33/324	
% of pre-/post-shut-in events	9/91	
Average M_w of pre-/post-events	−0.01/−0.05	
1st largest M_w event[a]	0.84, +97% (T), post	
2nd largest M_w event[a]	0.83, −45% (I), pre	
3rd largest M_w event[a]	0.75, −38% (I), post	
M_w range	−0.99 to 0.84	
Total Es	32 MJ	
Average M_w	−0.05	
Std. dev. M_w	0.30	
Cyclic 35 MPa residual injection		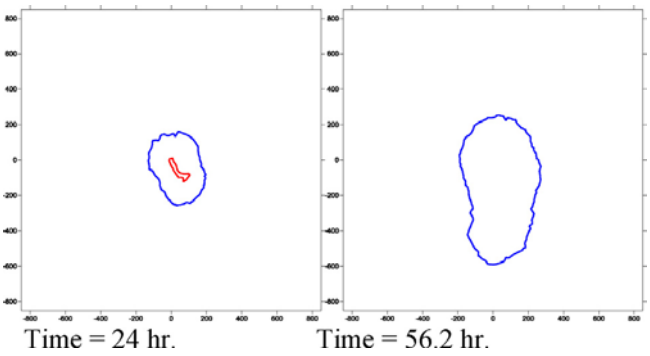
Total no. of events	67	
No. rock tensile/shear cracks	70/2	
No. joint tensile/shear cracks	–/–	
No. pre-/post-shut-in events	21/46	
% of pre-/post-shut-in events	31/69	
Average M_w of pre-/post-events	−0.18/−0.05	
1st largest M_w event[a]	0.51, −42% (I), pre	
2nd largest M_w event[a]	0.47, −45% (I), post	
3rd largest M_w event[a]	0.40, +19% (S), post	
M_w range	−0.70 to 0.51	
Total Es	5 MJ	
Average M_w	−0.09	
Std. dev. M_w	0.27	
Pulse type injection		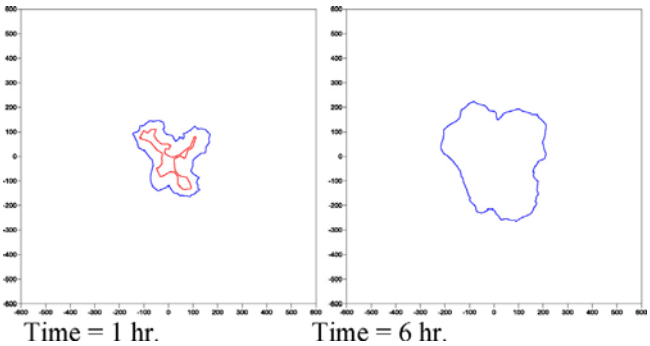
Total no. of events	128	
No. rock tensile/shear cracks	329/54	
No. joint tensile/shear cracks	–/–	
1st largest M_w event[a]	2.28, −60% (I), post	
2nd largest M_w event[a]	1.42, +60% (T), post	
3rd largest M_w event[a]	1.23, +35% (T), post	
M_w range	−0.56 to 2.28	
Total Es	207 MJ	
Average M_w	0.29	
Std. dev. M_w	0.35	

Table 2 (continued)

Pressure controlled simulations Intact reservoir		Fluid pressure distribution at indicated time (red: P_f = 75 MPa, blue: P_f = 0.1 MPa)
Monotonic injection		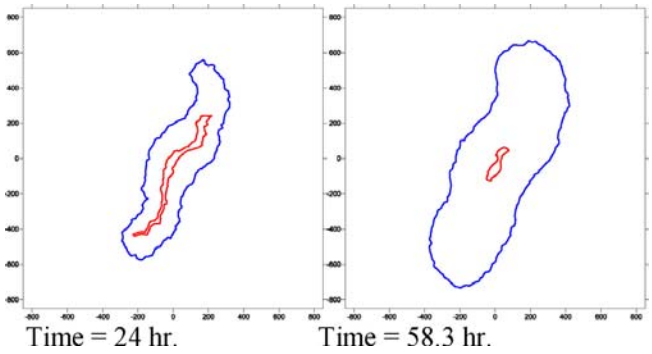
Total no. of events	489	
No. rock tensile/shear cracks	469/33	
No. joint tensile/shear cracks	0/32	
No. pre-/post-shut-in events	201/288	
% of pre-/post-shut-in events	41/59	
Average M_w of pre-/post-events	0.11/0.14	
1st largest M_w event[a]	1.06, -43% (I), post	
2nd largest M_w event[a]	1.03, +23% (S), post	
3rd largest M_w event[a]	0.96, +38% (T), post	
M_w range	−2.77 to 1.06	
Total Es	86 MJ	
Average M_w	0.12	
Std. dev. M_w	0.35	
Cyclic 5 MPa residual injection		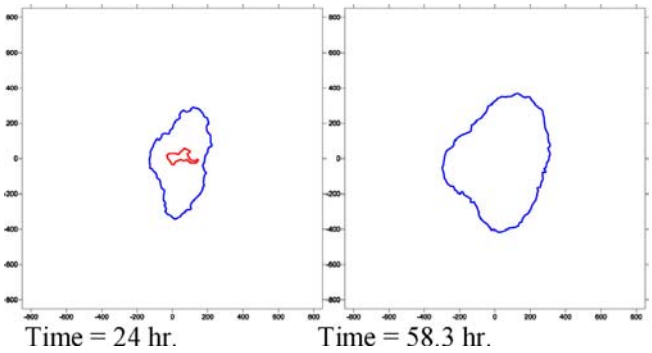
Total no. of events	268	
No. rock tensile/shear cracks	263/12	
No. joint tensile/shear cracks	1/27	
No. pre-/post-shut-in events	198/70	
% of pre-/post-shut-in events	74/26	
Average M_w of pre-/post-events	0.21/0.09	
1st largest M_w event[a]	0.97, -47% (I), pre	
2nd largest M_w event[a]	0.90, -17% (S), pre	
3rd largest M_w event[a]	0.89, -59% (I), pre	
M_w range	−0.57 to 0.97	
Total Es	49 MJ	
Average M_w	0.18	
Std. dev. M_w	0.27	
Cyclic 35 MPa residual injection		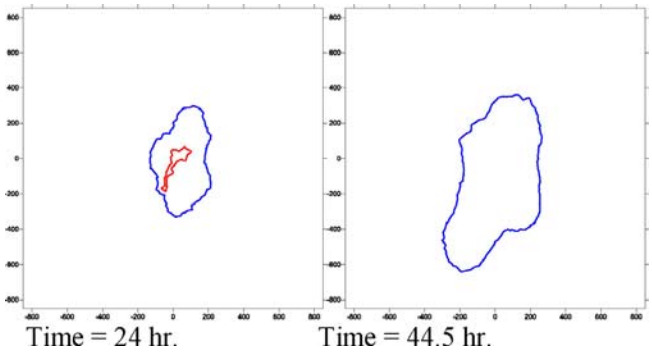
Total no. of events	337	
No. rock tensile/shear cracks	371/36	
No. joint tensile/shear cracks	0/29	
No. pre-/post-shut-in events	138/199	
% of pre-/post-shut-in events	41/59	
Average M_w of pre-/post-events	0.18/0.29	
1st largest M_w event[a]	1.80, −42% (I), post	
2nd largest M_w event[a]	1.54, −42% (I), post	
3rd largest M_w event[a]	1.29, +35% (T), post	
M_w range	−0.87 to 1.80	
Total Es	135 MJ	
Average M_w	0.24	
Std. dev. M_w	0.33	
Pulse type injection		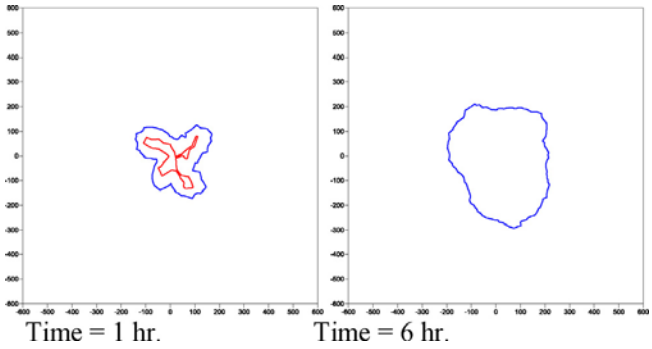
Total no. of events	223	
No. rock tensile/shear cracks	471/75	
No. joint tensile/shear cracks	0/40	
1st largest M_w event[a]	2.31, −60% (I), post	
2nd largest M_w event[a]	1.31, -33% (I), post	
3rd largest M_w event[a]	1.18, -39% (I), post	
M_w range	−0.45 to 2.31	
Total Es	264 MJ	
Average M_w	0.33	
Std. dev. M_w	0.32	

Table 2 (continued)

Pressure controlled simulations Intact reservoir		Fluid pressure distribution at indicated time (red: P_f = 75 MPa, blue: P_f = 0.1 MPa)
Sequentially increasing flow rate		
Total no. of events	468	
No. rock tensile/shear cracks	438/60	
No. joint tensile/shear cracks	1/34	
No. pre-/post-shut-in events	136/332	
% of pre-/post-shut-in events	29/71	
Average M_w of pre-/post-events	0.26/0.19	
1st largest M_w event[a]	1.01, -38% (I), post	
2nd largest M_w event[a]	0.96, -47% (I), post	
3rd largest M_w event[a]	0.94, -15% (S), pre	
M_w range	−0.84 to 1.01	
Total Es	100 MJ	
Average M_w	0.21	
Std. dev. M_w	0.30	
Max. P_f	136 MPa	
Total volume injected	270 m^3	
No. event $M_w > 0.9$	8 (pre: 3 / post: 5)	
Cyclically increasing flow rate		
Total no. of events	258	
No. rock tensile/shear cracks	247/26	
No. joint tensile/shear cracks	0/21	
No. pre-/post-shut-in events	194/64	
% of pre-/post-shut-in events	75/25	
Average M_w of pre-/post-events	0.17/0.09	
1st largest M_w event[a]	1.05, -36% (I), pre	
2nd largest M_w event[a]	0.97, +45% (T), post	
3rd largest M_w event[a]	0.93, -14% (S), pre	
M_w range	−1.10 to 1.05	
Total Es	48 MJ	
Average M_w	0.15	
Std. dev. M_w	0.31	
Max. P_f	118 MPa	
Total volume injected	374 m^3	
No. event $M_w > 0.9$	4 (pre: 2 / post: 2)	

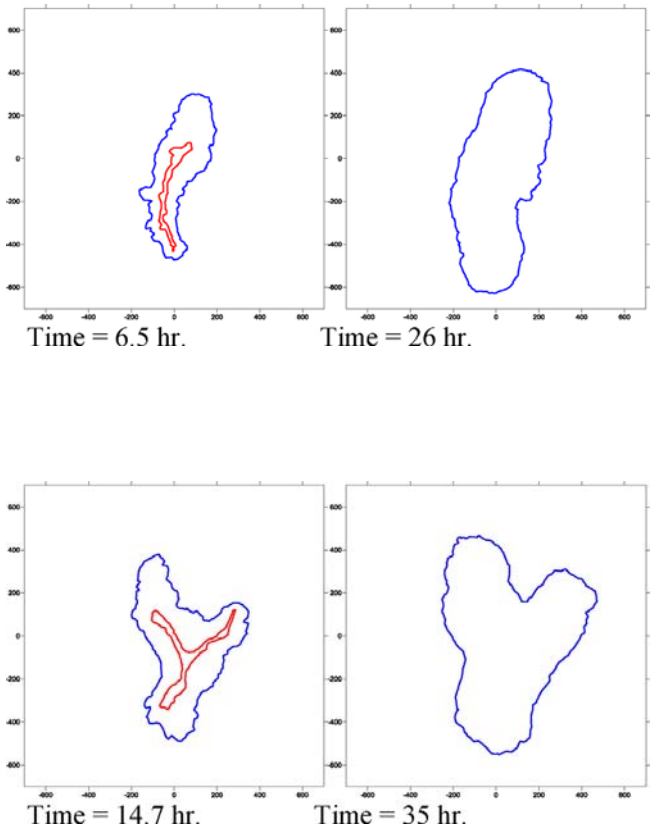

[a] Three largest magnitude events: moment magnitude M_w, R value of moment tensor, source mechanisms (T: tensile, S: shear, I: implosion), pre- or post-shut-in.

exclude any side effects on bond breakages coming from the kinetic seismic wave emanating from an induced bond breakage propagating outward and bouncing back when the wave is reflected at the boundary. Onset of Mode I and Mode II fractures of intact rock (enhanced parallel bond model) and pre-existing joint (smooth joint model) are governed by Mohr–Coulomb failure criterion (e.g. *Labuz and Zang*, 2012) where the parameters are listed in Table 1 and shown in Fig. 5.

Normal stress vs. shear stress at the parallel bonds and the smooth joint bonds after the in situ stresses are installed are plotted by (x) and (+) symbols. The (+) symbols scattered above the Mohr–Coulomb failure envelop for the pre-existing joint represents the failed smooth joint bonds while applying the in situ stresses.

Although we did not attempt to model the real Soultz-sous-Forêts stimulation case, the model parameters in particular for the intact rock strength properties are chosen such that they are approximately consistent with parameters observed for

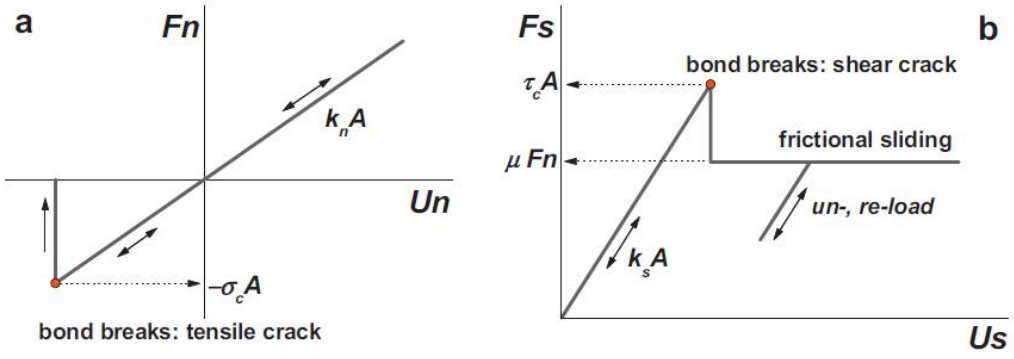

Figure 4. Force–displacement law for smooth joint bonded contacts: (a) normal force (Fn) vs. normal displacement (Un), (b) shear force (Fs) vs. shear displacement (Us) (k_n: normal stiffness, k_s: shear stiffness, σ_c: tensile strength, τ_c: shear strength, A: area of smooth joint cross section, μ: coefficient of friction against sliding).

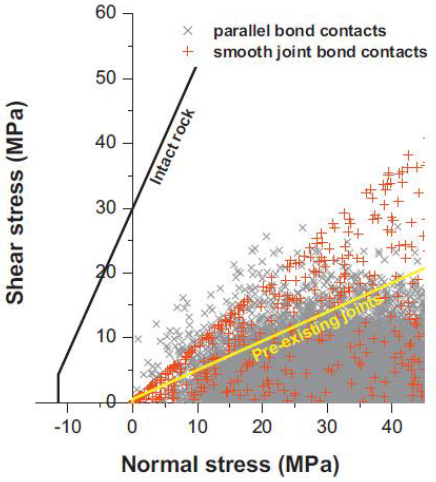

Figure 5. Mohr–Coulomb failure envelopes for intact rock (parallel bonded contacts) and pre-existing joints (smooth joint bonded contacts). Scattered data points are the normal stress vs. shear stress relations for the parallel bonds (black ×) and the smooth joint bonds (red +) after in situ stresses are installed. (For interpretation of the references to color in this figure legend, the reader is referred to the web version of this article.)

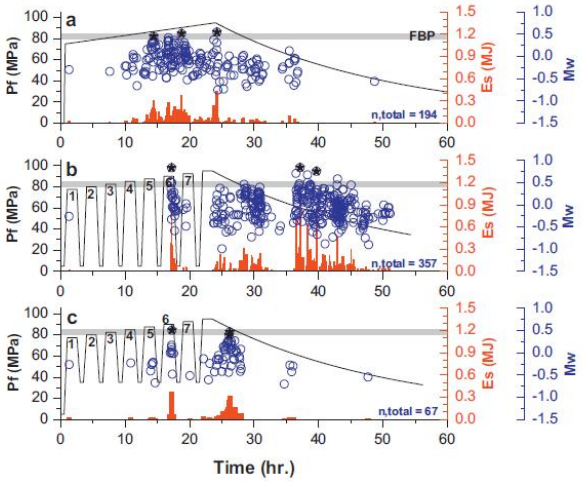

Figure 6. Stimulation of intact reservoirs. Simulated fluid pressure at the injection point (P_f) curves, seismic radiated energy Es and the moment magnitudes M_w of the induced events resulting from (a) monotonic injection, (b) cyclic 5 MPa residual injection and (c) cyclic 35 MPa residual injection. Black stars indicate the induced events with $M_w > 0.9$. Gray horizontal bar represents the fracture breakdown pressure estimates.

the Soultz granite.

Fracture breakdown pressure is estimated using the Haimson-Fairhurst equation (*Zang and Stephansson*, 2010), where the denominator is back-calculated from the injection pressure p^{HF} at the onset of near injection point induced events. The denominator approaches 2 for low-permeable hard rock, 1 for porous sedimentary rock. The denominator chosen (Table 1, $b = 1.44$) represents the porous nature of the model reservoir although the strength parameters (T_0: tensile strength, c: cohesion, ϕ: friction angle) resemble those of hard crystalline rock.

3.2. Modeling scenarios

For fixed in situ stresses (S_H = 75 and S_h = 60 MPa), intact and naturally fractured reservoirs are tested with four different types of injection schemes: (1) monotonic increase of fluid pressure at the injection point P_f (Figs. 6a and 11a), (2) cyclic increase of fluid pressure but lowered to 5 MPa between the cycles (Figs. 6b and 11b), (3) cyclic increase of fluid pressure but lowered to 35 MPa between the cycles (Figs. 6c and 11c), (4) pulse like increase of fluid pressure to 250 MPa (Fig. 16a and b) and decays. Except the pulse type injection, the fluid pressure at the injection point (P_f) is designed to reach 75 MPa within a short time and gradually increase to 95 MPa (Figs. 6a and 11a). Shut-in is simulated by reducing the P_f with time using negative exponential function. The pressure level at the first deflection point (75 MPa) is chosen as it is slightly larger than the sum of minimum horizontal stress (S_h) and rock tensile strength T_0, i.e. 60 + 11.5 ± 1.5 = 70–73 MPa. The chosen 95 MPa is higher than the estimated FBP (80–85 MPa), so to propagate the fracture further into the reservoir. The gradually increasing P_f at the injection point from 75 MPa to 95 MPa over 24 h represent an ideal case where the injection pressure is precisely controlled.

Two additional models are presented, where the fractured reservoir is subjected to two different types of flow rate controlled injections: (1) sequential increase of flow rate in three steps (10, 12.5, 15 l/s), (2) cyclic increase of flow rate in five cycles (5, 7.5, 10, 12.5, 15 l/s). In total, ten fluid injection scenarios are presented. Results of the pressure controlled fluid injections in intact and fractured reservoirs are presented in Sections 4.1 and 4.2, respectively. Pulse type pressure increase is discussed in Section 4.3. Section 4.4 deals with flow rate controlled injection.

4. Modeling results

Model results are summarized in Table 2: (1) total number of the induced events, (2) number of parallel bond breakages (rock failure) in Mode I (tensile) and in Mode II (shear), (3) number of smooth joint bond breakages (joint failure) in Mode I (tensile) and in Mode II (shear), (4) number of pre-shut-in and post-shut-in induced events, (5) percentage of number of pre- and post-shut-in induced events, (6) average of moment magnitude M_w of the pre- and post-shut-in induced events, (7) information of the three largest magnitude events: moment magnitude M_w, R value of the moment tensor and the source mechanisms (T: tensile, S: shear, I: implosion) and the period when it occurred (pre- or post-shut-in), (8) range of moment magnitude M_w of the induced events, (9) total seismic radiated energy Es, (10) average moment magnitude M_w and (11) standard deviation of the moment magnitude M_w of the induced events. For the flow rate controlled simulations, following information is additionally provided: (1) maximum fluid pressure P_f, (2) total volume of fluid injected, (3) number of induced events of which M_w is larger than 0.9 and their populations during pre- and post-shut-in periods. Two figures for each tested scenario are provided showing the distributions of the fluid pressure at the selected times. Blue and red contours are the iso-lines where the fluid pressure is 0.1 MPa and 70 MPa, which represent the fluid migration front and the high fluid pressurized zone, respectively.

4.1. Stimulation of intact reservoir – pressure controlled injection

Fig. 6 shows the modeling data: simulated fluid pressure (P_f) at the injection point, moment magnitudes M_w and seismic radiated energy Es of the induced events in the intact reservoirs subjected to (a) monotonically increasing P_f (referred to hereafter as 'Monotonic injection'), (b) cyclically increasing P_f but lowered to 5 MPa between the cycles (referred to hereafter as 'Cyclic 5 MPa residual injection') and (c) cyclically increasing P_f but lowered to 35 MPa between the

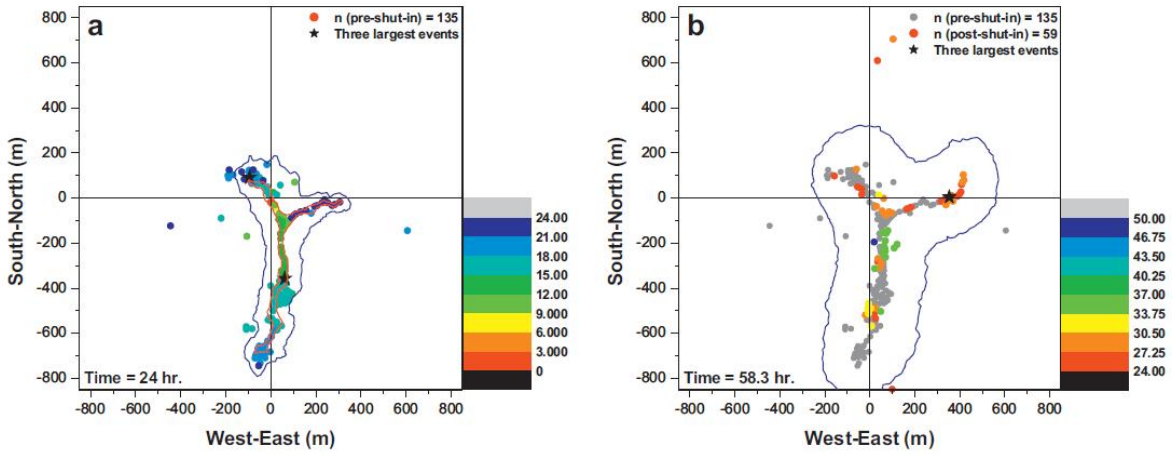

Figure 7. Spatio-temporal distributions of the induced seismic events in intact reservoir during (a) pre-shut-in and (b) post-shut-in, resulting from monotonic injection (Fig. 6a). Color represents the occurrence time (in hour) of the events. In (b), pre-shut-in events are displayed in gray dots. Distribution of fluid pressures of 0.1 MPa and 70 MPa are indicated by blue and red contours, respectively. Time of the fluid pressure contours is indicated at the bottom left corner. Injection point is at model origin. Black stars are the three largest magnitude events. (For interpretation of the references to color in this figure legend, the reader is referred to the web version of this article.)

cycles (referred to hereafter as 'Cyclic 35 MPa residual injection').

4.1.1. Monotonic injection

Fig. 6a shows that intense fracturing starts at 10 h when the P_f approaches FBP (gray horizontal bar). Moment magnitudes M_w of the induced events are all under 0.6. Compared to the pre-shut-in events, M_w of the post-shut-in events are lower. The three largest M_w events all occurred in the pre-shut-in period (black stars in Fig. 6a). Fracturing process is documented in Fig. 7a for the pre-shut-in events and Fig. 7b for the post-shut-in events. Color represents the time of occurrence. Two contours are drawn for the fluid pressure which indicate 70 MPa and 0.1 MPa for the red and the blue lines, respectively, at the indicated times. Inner region of the red contour implies high fluid pressure (>70 MPa) area, whereas outer region of the blue contour implies low fluid pressure (<0.1 MPa) area.

In general, hydraulically driven fracture grows in NS direction (parallel to S_H). However, the fracture propagation pattern is not symmetric and shows longer propagated path to S than to N. Such asymmetric fracture growth is due to heterogeneity nature of the discrete element model, i.e. randomly chosen particle size hence packing fabric and non-uniform bond strength parameters. In the spatio-temporal distributions of the pre- and the post-shut-in events (Fig. 7a and b), the three largest magnitude events are marked by black stars.

4.1.2. Cyclic 5 MPa residual injection

Fluid pressure curve is changed to cyclic style where pressure increase and decrease is repeated in seven cycles until it reaches 95 MPa then decays. Between the cycles, P_f is lowered to 5 MPa (Fig. 6b). Such repeated increasing and decreasing of P_f represents a reservoir stimulation operation with fluid injection followed by massive withdrawal so that the fluid pressure at the injection point returns to the initial pressure level. Unlike in monotonic injection, events are occurring at ca. 17 h, which might be due to insufficient duration time where the fluid pressure is maintained at high levels. Fracture pattern is documented in Fig. 8. During stimulation, repeated pressurizing and depressurizing results in anisotropic shape of the induced event cloud longer in S_h direction. After shut-in, however, fracture significantly grows in NS with slight deviation (5–10°).

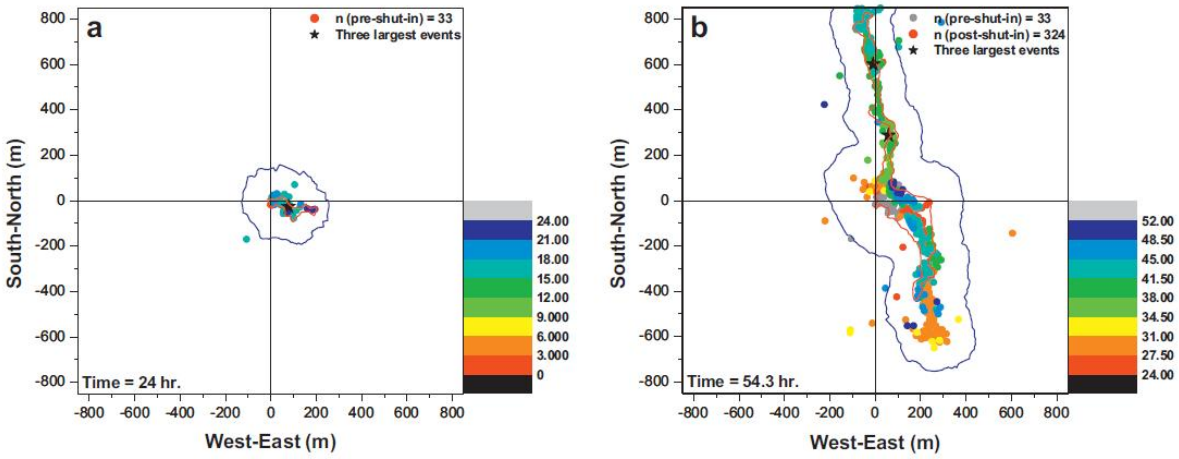

Figure 8. Spatio-temporal distributions of the induced seismic events in intact reservoir during (a) pre-shut-in and (b) post-shut-in, resulting from cyclic 5 MPa residual injection (Fig. 6b). Color represents the occurrence time (in hour) of the induced events. In (b), pre-shut-in events are displayed in gray dots. Distribution of fluid pressures of 0.1 MPa and 70 MPa are indicated by blue and red contours, respectively. Time of the fluid pressure contours is indicated at the bottom left corner. Injection point is at model origin. Black stars are the three largest magnitude events. (For interpretation of the references to color in this figure legend, the reader is referred to the web version of this article.)

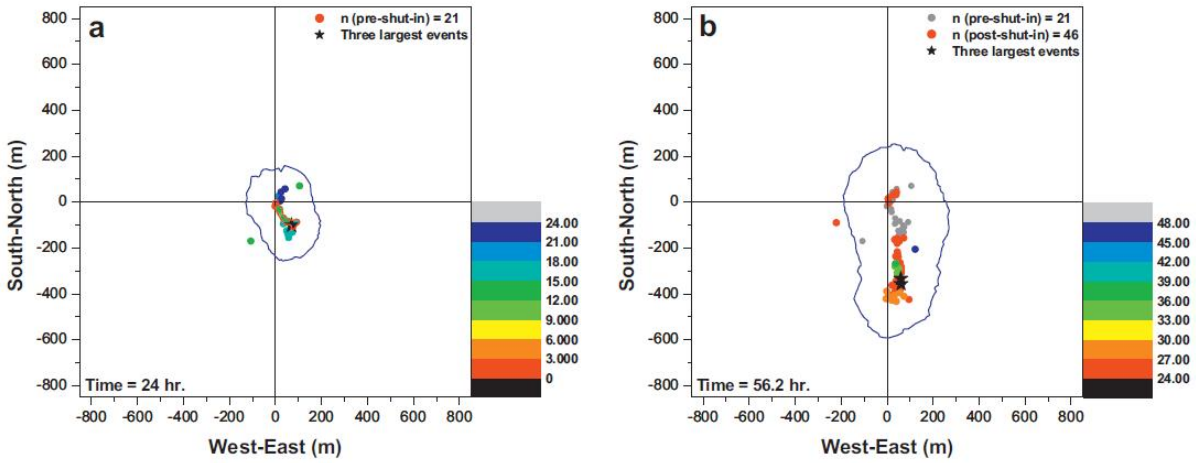

Figure 9. Spatio-temporal distribution of the induced seismic events in intact reservoir during (a) pre-shut-in and (b) post-shut-in, resulting from cyclic 35 MPa residual injection (Fig. 6c). Color represents the occurrence time (in hour) of the induced events. In (b), pre-shut-in events are displayed in gray dots. Distribution of fluid pressures of 0.1 MPa and 70 MPa are indicated by blue and red contours, respectively. Time of the fluid pressure contours is indicated at the bottom left corner. Injection point is at model origin. Black stars are the three largest magnitude events. (For interpretation of the references to color in this figure legend, the reader is referred to the web version of this article.)

4.1.3. Cyclic 35 MPa residual injection

Cyclic style of injection is further changed so that the P_f decreases to 35 MPa between the cycles. Similar to the previous scenario, cyclic 35 MPa residual injection represents a stimulation operation with fluid injection followed by partial withdrawal. Unlike in the previous case, total number of induced events is much less (n = 67, previously n = 357). From Fig. 9, the extent of the fracture propagated length (ca. 500 m in NS) is less than half of the total length in the previous case (ca. 1600 m in NS). Both cyclic injection schemes resulted in more post-shut-in induced events. However, cyclic 5 MPa residual injection resulted in significantly larger amount of the post-shut-in events. This difference might be due to the larger difference between the high and low levels of fluid pressure applied at the injection point. It is interpreted that the cyclic injection is similar to fatigue loading and the 5 MPa residual injection represents high amplitude fatigue. It is interpreted that the strength of a material subjected to high amplitude fatigue loading is significantly reduced, compared to low amplitude fatigue loading (35 MPa residual injection).

Distributions of the M_w of the induced events from the three scenarios are shown in Fig. 10. In general, the histograms follow Gaussian distribution. Closer resemblance to the exponential distribution can be achieved when the seismicity algorithm is expanded to compute the moment magnitudes of the slipping events. Moment magnitudes vs. cumulative frequency relations of the induced events show similar patterns to the Gutenberg-Richter law.

4.2. Stimulation of fractured reservoir – pressure controlled injection

Fig. 11 shows the modeling results: simulated fluid pressure (P_f) at the injection point, moment magnitudes M_w and seismic radiated energy Es of the induced events, in the fractured reservoir subjected to (a) monotonic injection, (b) cyclic 5 MPa residual injection, and (c) cyclic 35 MPa residual injection.

4.2.1. Monotonic injection

Fig. 11a shows that the induced events occur at ca. 5 h, earlier than in intact reservoir case. This is due to the presence and failure (re-activation) of the pre-existing joints that have much lower strength than the intact rock matrix strength. Intense fracturing begins at 15 h. Average magnitudes of the pre-shut-in and the post-shut-in events are 0.11 (n = 201) and 0.14 (n = 288), respectively. Unlike in the intact reservoir case (Fig. 6a), the three largest events with $M_w > 0.9$ occurred in the post-shut-in period. Fracturing process is documented in Fig. 12a for the pre-shut-in events and Fig. 12b for the post-shut-in events. During stimulation, dominating fracturing mechanism is Mode I tensile fractures of the intact rock that propagated in NE-SW (Table 2, n = 469 for tensile cracks, n = 33 for shear cracks). As the propagating fracture tip approaches the zone of dense pre-existing joints, it results in Mode II shear failure of the pre-existing joints, i.e. re-activation of the pre-existing joints (Table 2, n = 0 for tensile cracks, n = 32 for shear cracks). Moment magnitudes of the three largest post-shut-in events are 1.06, 1.03 and 0.96. Source mechanisms of the three largest magnitude events are determined as implosion (1.06), shear (1.03) and tensile (0.96). This result is contrary to what is usually believed in seismology that most of the large magnitude events have shearing (double-couple) mechanism. Fig. 12b shows that the post-shut-in large magnitude events occurred at the outer-rim of the event cloud generated in the pre-shut-in period. Frac-

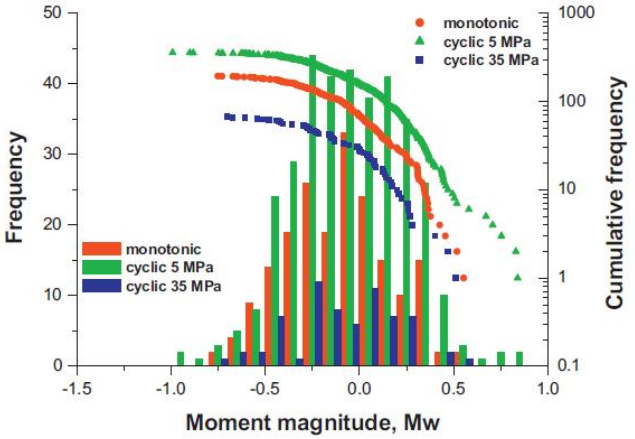

Figure 10. Histograms (left) of the moment magnitudes of the induced seismic events in intact reservoirs and their magnitude vs. cumulative frequency distribution (right) resulting from monotonic injection (red), cyclic 5 MPa residual injection (green) and cyclic 35 MPa residual injection (blue). (For interpretation of the references to color in this figure legend, the reader is referred to the web version of this article.)

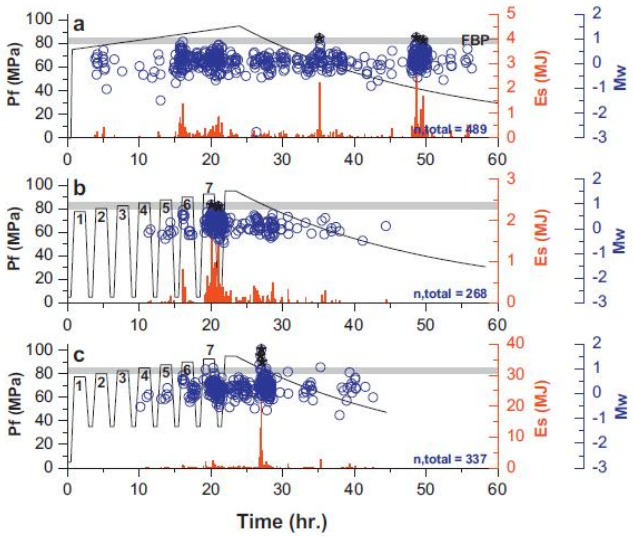

Figure 11. Stimulation of fractured reservoirs. Simulated fluid pressure at the injection point (P_f) curves, seismic radiated energy Es and the moment magnitudes M_w of the induced events resulting from (a) monotonic injection, (b) cyclic 5 MPa residual injection and (c) cyclic 35 MPa residual injection. Black stars indicate the induced events with $M_w > 0.9$.

ture propagates sub-vertically, i.e. NNE-SSW, which is slightly deviated from the S_H direction due to the presence of the pre-existing joints. The extent of fracture propagation length in NE-SW is similar.

4.2.2. Cyclic 5 MPa residual injection

Same as earlier, P_f curve is changed to cyclic style where pressure increase and decrease is repeated in seven cycles until it reaches 95 MPa then decays. Between the cycles, P_f is lowered to 5 MPa. Unlike in monotonic injection (Fig. 11a) where the events are induced in the entire time range, almost all induced events occurred during time interval between 10 and 40 h. Induced event cloud in the pre-shut-in period shows longer extent in NS (Fig. 13a). Moreover there are many induced events at the pre-existing joints and far outside of the 0.1 MPa fluid pressure contour. This implies that the reactivation of the pre-existing joints can take place by smaller pore fluid pressure perturbation (<0.1 MPa). Spatio-temporal distribution of the post-shut-in induced events is plotted in Fig. 13b. Events are induced at the outer-rim of the pre-shut-in event cloud, not at the NS tips but EW of the event cloud. This results in overall isotropic shape of the event cloud. The three largest events are 0.97, 0.90 and 0.89, marked by black stars (Fig. 13a). Kaiser effect is observed at the 5th-7th cycles where events are induced when the P_f exceeds the previous maximum pressure level and even after the P_f falls to 5 MPa. This is due to that P_f has far exceeded the FBP and the reservoir already entered into uncontrollable state.

4.2.3. Cyclic 35 MPa residual injection

Cyclic style of injection is changed so that P_f is maintained at 35 MPa between the cycles. Similar to previous scenario, Kaiser effect is observed at the 5th-7th cycles where events are induced when the P_f exceeds the previous maximum pressure level. Dense event cloud is formed during 25–30 h (Fig. 11c). The simulation is stopped at 45 h, as numerical error (divergence problem) occurred. Three largest events (M_w = 1.80, 1.54, 1.29) all occurred in the post-shut-in period and are located within the 0.1 MPa fluid pressure contour and at densely jointed area (Fig. 14b).

Distributions of the moment magnitudes of all the induced events from the three tested scenarios are shown in Fig. 15. Similar to the intact reservoirs, the histograms follow Gaussian distribution. Moment magnitude vs. cumulative frequency relations show similar pattern to the Gutenberg-Richter law. Least square of maximum likelihood methods can be applied to determine the Gutenberg-Richter law parameters, e.g. b-value. Seismic moment and moment magnitude depend on the particle size. However, the minimum M_w simulated are all different. This implies that the M_w statistics are not biased due to the particle size, but depends solely on the failure mechanisms and amount of strain energy released at the bond failure.

4.3. Stimulation of intact and fractured reservoirs under pulse type fluid injection

Unlike in previous scenarios, this section deals with stimulation of reservoir using pulse type fluid injection, i.e. P_f increases rapidly beyond the FBP. Fig. 16 shows the simulated P_f curve, radiated seismic energy Es and the moment magnitudes M_w of the induced events with respect to time in (a) the intact reservoir and in (b) the fractured reservoir.

The largest magnitude event (M_w = 2.28) occurred with

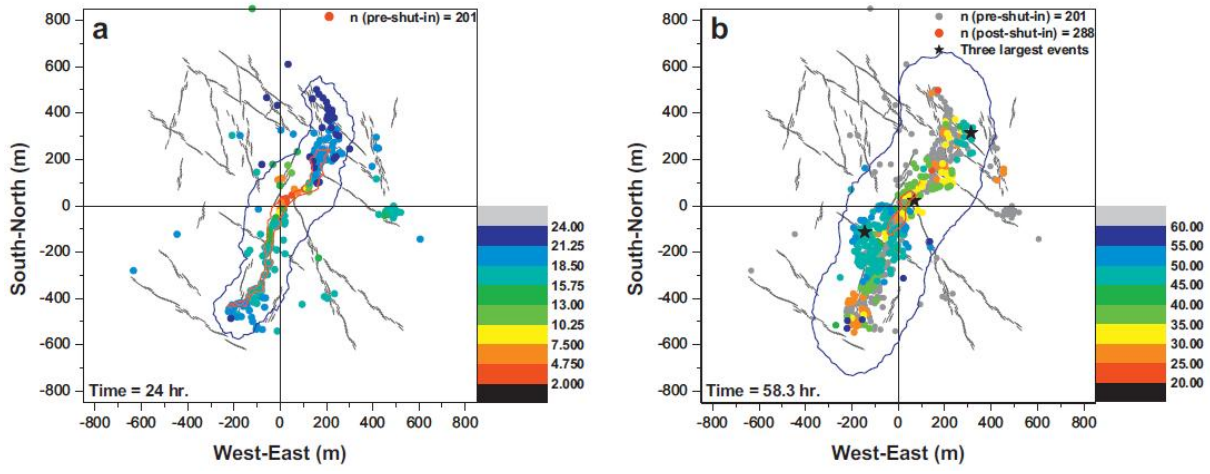

Figure 12. Spatio-temporal distribution of the induced seismic events in fractured reservoir during (a) pre-shut-in and (b) post-shut-in, resulting from monotonic injection (Fig. 11a). Color represents the occurrence time (in hour) of the induced events. In (b), pre-shut-in events are displayed in gray dots. Distribution of fluid pressures of 0.1 MPa and 70 MPa are indicated by blue and red contours, respectively. Time of the fluid pressure contours is indicated at the bottom left corner. Injection point is at model origin. Black stars are the three largest magnitude events. (For interpretation of the references to color in this figure legend, the reader is referred to the web version of this article.)

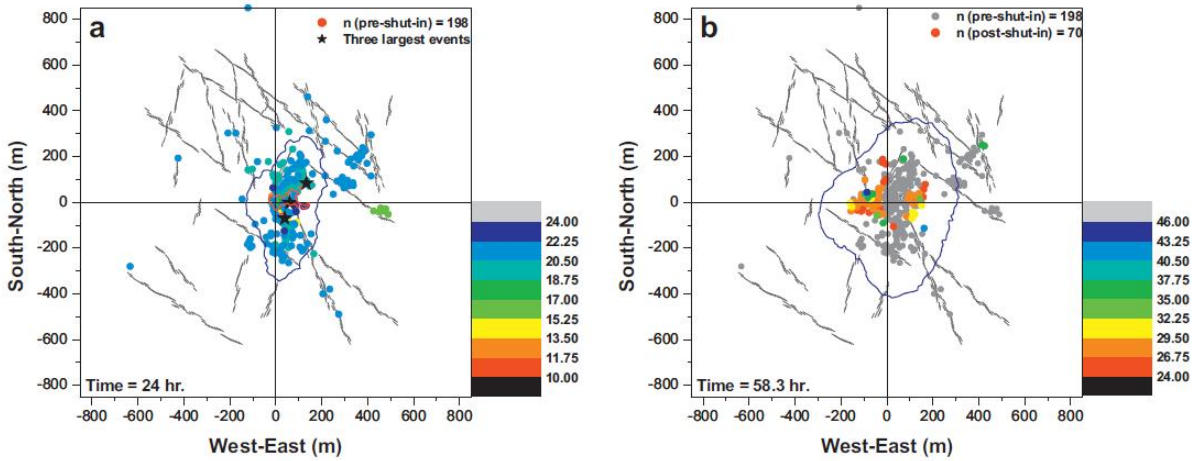

Figure 13. Spatio-temporal distribution of the induced seismic events in fractured reservoir during (a) pre-shut-in and (b) post-shut-in, resulting from cyclic 5 MPa residual injection (Fig. 11b). Color represents the occurrence time (in hour) of the induced events. In (b), pre-shut-in events are are displayed in gray dots. Distribution of fluid pressures of 0.1 MPa and 70 MPa are indicated by blue and red contours, respectively. Time of the fluid pressure contours is indicated at the bottom left corner. Injection point is at model origin. Black stars are the three largest magnitude events. (For interpretation of the references to color in this figure legend, the reader is referred to the web version of this article.)

0.62 h delay from the time of peak P_f. No seismicity is observed after 2.5 h (Fig. 16a). Fig. 17a shows the spatio-temporal distribution of the induced events in the intact reservoir. Color represents the occurrence time of the events, i.e. early events in red and late events in blue. Three contours are provided which show the 0.1 MPa fluid pressure distributions at the indicated times (1, 3, 6 h). The figure indicates that the event cloud emerges at the model center and grows in isotropic pattern. Red events are concentrated at the model center (occurrence time: 0–1 h) followed by orange events (occurrence time: 1–2 h).

Fractured reservoir behaves more or less in same manner, which are (i) occurrence of the largest magnitude events with hypocenters near the injection point with some delay time from the peak P_f , (ii) isotropic growth pattern of the induced event cloud, and (iii) occurrences of the induced events ahead of the 0.1 MPa fluid pressure contour. However, locations of the induced events during 1–2 h (orange colored) extend much further from the injection point. These events are induced mostly by the elastic wave generated by the pulse like pressure increase rather than by the increased fluid pressure. Several events induced during 4–7 h (light blue, blue, and purple colored) occurred within the fluid pressure contours. These events are induced by the increased fluid pressure. Event occurrence lasts longer than in the intact reservoir as migration of the pressurized fluid causes re-activation of the pre-existing joints. This is different from the models presented in Sections 4.1 and 4.2, where the location of event occurrence is mostly confined within the 0.1 MPa fluid pressure contours.

Under pulse type fluid pressure injection, occurrence of the induced events ahead of the fluid pressure contours (fore front induced events, FFIE) is more pronounced. This is due to the elastic wave generated by the pulse pressurizing at the injection and travels faster than the speed of fluid migration. More FFIE are observed in the fractured reservoir (Fig. 17b) than in the intact reservoir (Fig. 17a), as they are mostly re-activation of the pre-existing joints.

The moment magnitudes of the largest events in both models are above 2, which are far greater than the average magnitude (Table 2). The source mechanisms of these events are all implosion. This implies that when such pulse type injection is applied to a reservoir as a stimulation treatment, it may act like a detonation and the elastic wave generated by the pulse can cause pore collapses which are then documented as

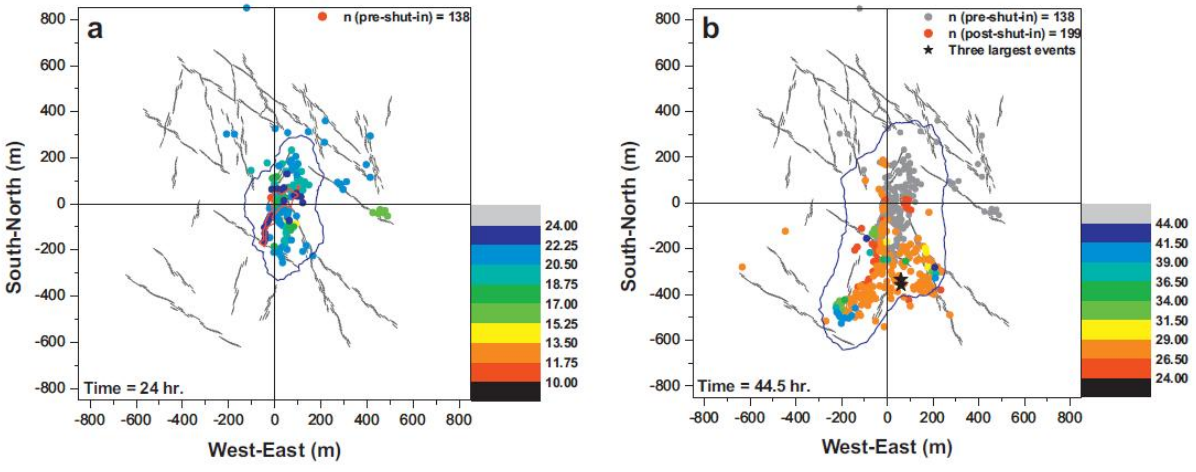

Figure 14. Spatio-temporal distribution of the induced seismic events in fractured reservoir during (a) pre-shut-in and (b) post-shut-in, resulting from cyclic 35 MPa residual injection (Fig. 11c). Color represents the occurrence time (in hour) of the induced events. In (b), pre-shut-in events are displayed in gray dots. Distribution of fluid pressures of 0.1 MPa and 70 MPa are indicated by blue and red contours, respectively. Time of the fluid pressure contours is indicated at the bottom left corner. Injection point is at model origin. Black stars are the three largest magnitude events. (For interpretation of the references to color in this figure legend, the reader is referred to the web version of this article.)

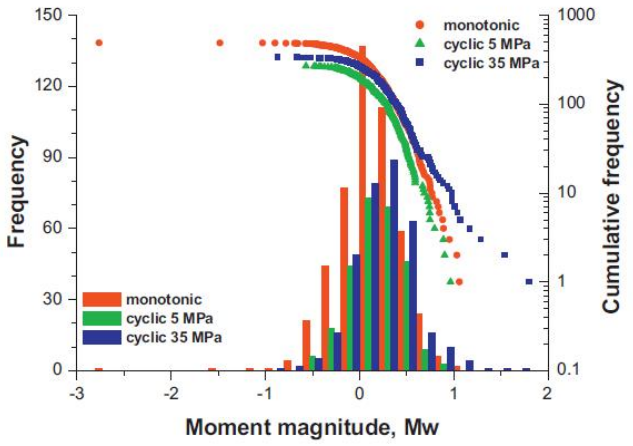

Figure 15. Histograms (left) of the moment magnitudes of the induced seismic events and their magnitude vs. cumulative frequency distribution (right) resulting from monotonic injection (red), cyclic 5 MPa residual injection (green), cyclic 35 MPa residual injection (blue). (For interpretation of the references to color in this figure legend, the reader is referred to the web version of this article.)

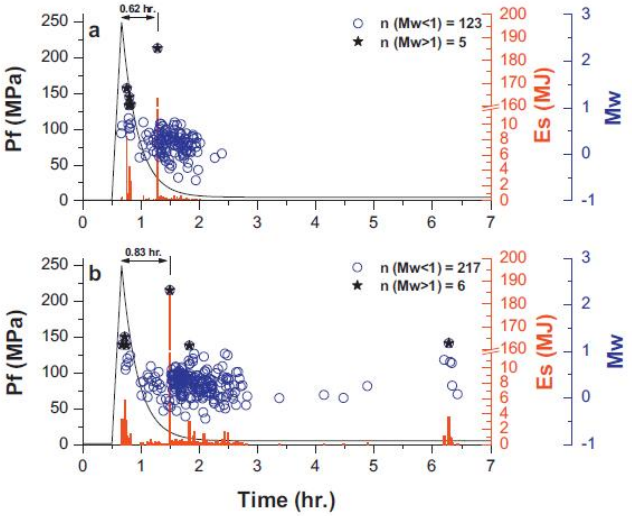

Figure 16. Simulated fluid pressure at the injection point (P_f) curves, seismic radiated energy Es and the moment magnitudes M_w of the induced events in (a) intact and (b) fractured reservoirs resulting from pulse type injection.

implosion source events. In the intact reservoir, the source mechanism of the second and the third largest events are tensile. This implies that the rock mass which was heavily compressed by the pulse tends to expand rapidly, which then results in tensile events.

These two simulations show that the pulse type fluid injection may not be desirable for developing an EGS in both intact and naturally fractured reservoirs, as it tends to result in (i) induced events with M_w far above the average level (Table 2), which is potentially a threat to the environment and (ii) relatively small and isotropic pattern of induced event cloud under anisotropic in situ stress condition, and (iii) large magnitude events with implosion source (pore collapsing) which may result in reduction of reservoir permeability.

4.4. Flow rate controlled fluid injection

This section deals with flow rate controlled fluid injection into a fractured reservoir. Two types of injection scenarios are tested: (1) sequentially increasing flow rate in three steps, (2) cyclically increasing flow rate.

4.4.1. Sequentially increasing rate injection

Fig. 18 shows the flow rate increase in three steps (10, 12.5, 15 l/s) maintained for 2 h each, P_f at the injection point, seismic radiated energy Es and moment magnitudes M_w of the induced events. Comparing with typical field observation, a few similarities are found: (1) instantaneous increase of the P_f with flow rate increase, (2) instantaneous drop of fluid pressure with event occurrence, (3) decreasing fluid pressure at the onset of shut-in, (4) less frequent event occurrence rate in the post-shut-in period, and (5) large magnitude events in the post-shut-in period.

The applied rates of injection are low compared to actual rates of injection applied in Soultz EGS, e.g. 30–50 l/s (*Cuenot et al.*, 2008). As mentioned earlier, we did not attempt to model the real Soultz-sous-Forêts stimulation case. However, we adopted the injection style where the injection rate is increased step-wise. Ongoing research aims at simulating the actual injection rates in 3D model calibrated against the Soultz EGS.

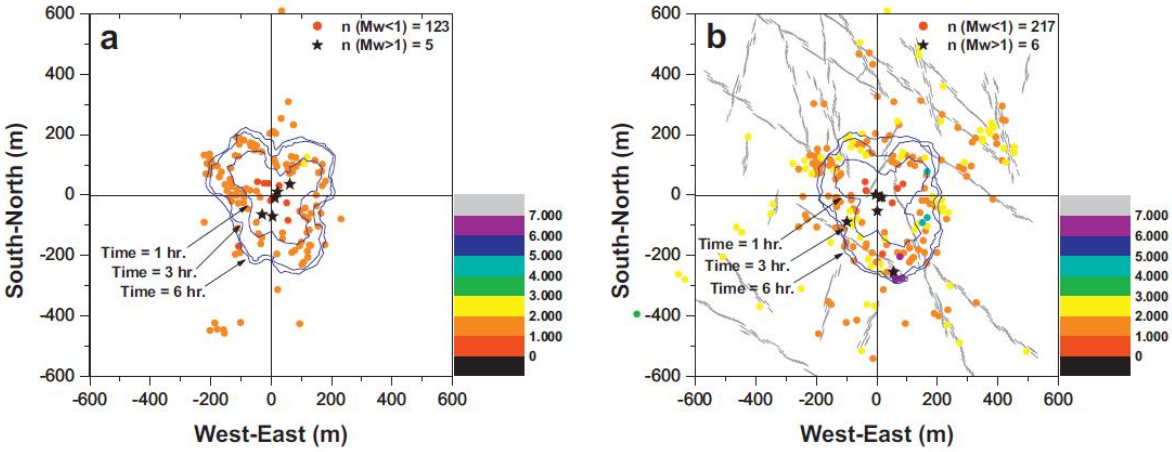

Figure 17. Spatial and temporal distribution of the induced seismic events in (a) intact and (b) fractured reservoirs resulting from pulse type injection Color represents the occurrence time (in hour) of the induced events. Distribution of fluid pressures of 0.1 MPa at several selected time is indicated by blue contour. Injection point is at model origin. Black stars are the events with $M_w > 1$. (For interpretation of the references to color in this figure legend, the reader is referred to the web version of this article.)

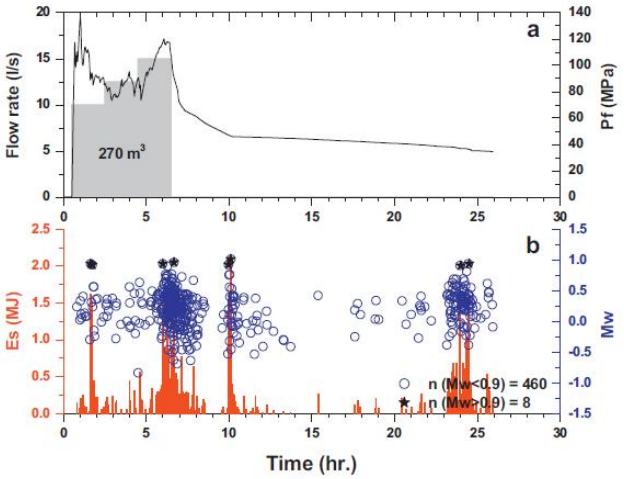

Figure 18. (a) Flow rate controlled injection with sequentially increasing rates (10, 12.5, 15 l/s) and the fluid pressure at the injection point (P_f). (b) Seismic radiated energy Es and the moment magnitudes M_w of the induced events vs. time. Black stars indicate the induced events with $M_w > 0.9$.

Spatio-temporal distributions of the induced events are plotted in Fig. 19a and b for the pre- and the post-shut-in events, respectively. Color indicates the time of occurrence, i.e. early events in red and late event in blue. Fracture initiates near the injection point and propagates mostly downward and turn its direction from SW to SE. Most of the events are confined within the fluid pressure distribution contour indicating that the major driving force for the event occurrence is the increased fluid pressure. However, a few events occurred outside of the fluid pressure contour. These events are mostly at the pre-existing joints and indicate that re-activation of the pre-existing joints can occur by small perturbation (<0.1 MPa) of the fluid pressure.

Post-shut-in events are plotted in Fig. 19b. The events are induced by migration of the pressurized fluid. Events occurred during 6–9.5 h (red and orange colored) are widely distributed and mostly at the pre-existing joints. The time range between 6 and 9.5 h is where the P_f at the time of shut-in (120 MPa) decreased rapidly to 50 MPa. Such rapid relaxation caused shock in the reservoir and resulted in many events induced at the pre-existing joints that are even far away from the injection point. Gray stars are the induced events with the $M_w > 0.9$, which occurred within and at outer-rim of the event cloud and far away from the injection point but at the pre-existing joints. The results agree well with the field observations made by *Mukuhira et al.* (2013) on Basel EGS induced seismicity cloud. They observed that the large events during the stimulation and just after bleeding off had hypocenters within the seismic event cloud while the large events that occurred long after shut-in were located outside of the seismic event cloud.

4.4.2. Cyclically increasing rate injection

Flow rate is increased cyclically from 5 l/s to 15 l/s divided into 5 cycles with 1 l/s of flow rate maintained between the cycles (Fig. 20a). In this scenario, after the injection rate is increased in each cycle, Kaiser effect is observed. It is manifested when the fluid pressure P_f exceeds previous maximum pressure after the injection rate is increased. The times when the P_f exceeds the previous maximum in each cycle and the events occurred are indicated by the red triangles at the upper abscissa of Fig. 20a. It should be noted that there is a delay in P_f increase when the injection rate is increased. This amount of delay time corresponds to the travel time of the fluid from the injection point to the tips of the propagated fractures. Unlike the previous injection scenario, the fluid pressure curve shows slow relaxation after shut-in, i.e. time taken for lowering the P_f from 113 MPa to 50 MPa is ca. 8 h. During this time range (14–22 h) only 41 events are induced which is 17% of the number of induced events in the previous scenario. This implies that controlling the speed of fluid pressure relaxation in the post-shut-in period can play a significant role in mitigating the effects of large magnitude induced events.

Spatio-temporal distributions of the induced events are plotted in Fig. 21a and b for the pre- and the post-shut-in events, respectively. Color represents the time of occurrence, i.e. early events in red and late event in blue. Fracture starts at the injection point (red events) and propagates downward in SE. It stops then two branching fractures are developed and propagated in NE and SSW directions, toward the pre-existing joints. This is due to the insufficient energy to propagate the fracture further into the intact rock. Instead, the two branching fractures are formed toward the pre-existing joints. Post-shut-in events are

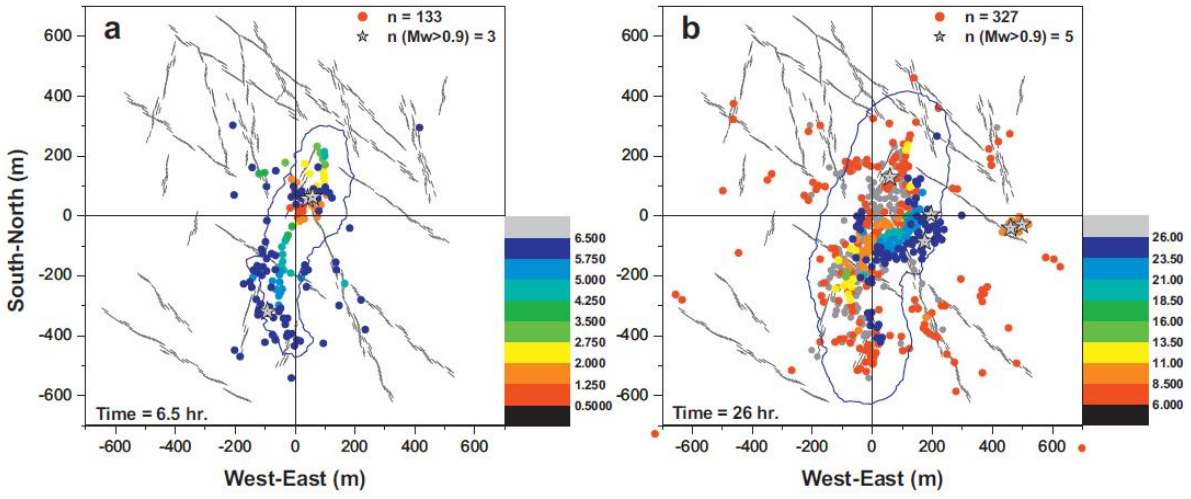

Figure 19. Spatio-temporal distributions of the induced seismic events in fractured reservoir during (a) pre-shut-in and (b) post-shut-in, resulting from sequentially increasing rate injection. Color represents the occurrence time (in hour) of the induced events. In (b), pre-shut-in events are displayed in gray dots. Distribution of fluid pressures of 0.1 MPa and 70 MPa are indicated by blue and red contours, respectively. Time of the fluid pressure contours is indicated at the bottom left corner. Injection point is at model origin. Gray stars are the events with $M_w > 0.9$. (For interpretation of the references to color in this figure legend, the reader is referred to the web version of this article.)

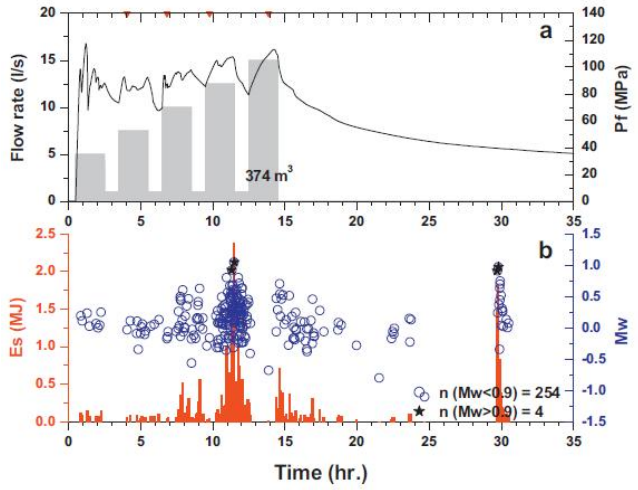

Figure 20. (a) Flow rate controlled injection with cyclically increasing rates (5, 7.5, 10, 12.5, 15 l/s) and the fluid pressure at the injection point (P_f). (b) Seismic radiated energy Es and the moment magnitudes M_w of the induced events vs. time. Black stars indicate the induced events with $M_w > 0.9$.

plotted in Fig. 21b. Compared to the previous scenario, the events with $M_w > 0.9$ occurred near the injection point. The two large magnitude events in the pre-shut-in period (near coordinate $x = 450, y = -50$) are also observed in the previous scenario. However, unlike in the previous scenario, these two events are induced during stimulation.

Distributions of the moment magnitudes of all the induced events from the two tested scenarios are shown in Fig. 22. Similar to Figs. 10 and 15, the histograms follow Gaussian distribution and the moment magnitude vs. cumulative frequency relations are similar to the Gutenberg-Richter law.

Comparing the two injection scenarios, it shows that the cyclic injection results in (Table 2): (i) larger volume of injected fluid (270 m^3 vs. 374 m^3), (ii) slower relaxation of the fluid pressure after shut-in (3.5 h vs. 8 h to lower the peak P_f at the time of shut-in to 50 MPa), (iii) less number of total events (468 vs. 258) and larger magnitude events (8 vs. 4 of $M_w >$ 0.9), (iv) less portion of the post-shut-in induced events (71% vs. 25%), (v) larger fluid saturated area. The results imply that the cyclic stimulation treatment shows potential in mitigating the effects of larger magnitude events. However, how much the reservoir permeability can be enhanced should be further investigated, and advances are being made regarding this issue (*Zang et al.*, 2013).

5. Discussion

There are a few issues which require discussion. First question is why the intact reservoir under cyclic 5 MPa residual injection produced induced events mostly in the post-shut-in period (Fig. 6b), i.e. even when P_f is decreasing. This is thought to be a consequence of many times of repeated pressurizing and depressurizing (down to 5 MPa), which may have acted as a fatigue loading. This implies that when creating/optimizing an EGS in reservoir rock mass which is intact or with relatively low density and low persistent joints, performing repeated pressuring-depressurizing at the injection point may be desirable. However the pressure level between the cycles should be properly chosen as cyclic 35 MPa residual injection produces shorter fracture propagation length (Fig. 9).

Second question raised is, on the contrary, then why the fractured reservoir under same cyclic injection exhibited less anisotropic event cloud (Fig. 13). One possible reason can be that a large portion of the energy given to the reservoir by the repeated pressurizing-depressurizing at the injection point is consumed by silent sliding at the pre-existing joints. Therefore, when creating an EGS in a naturally fractured rock mass, repeated pressurizing-depressurizing of the reservoir may not be a solution. In such case, as shown in Fig. 13, increasing the injection pressure continuously but slowly may result in more optimized heat exchanger.

Fig. 23 shows temporal changes of the two principal stresses (σ_1 and σ_2) monitored within 320 m radius area around the injection point in the (a) intact and (b) fractured reservoirs subjected to the pressure controlled cyclic 5 MPa residual injection. For monitoring the stresses, we used the measurement circle approach in PFC^{2D} which keeps track of the areal averaged stress components (σ_{xx}, σ_{xy}, σ_{yx}, σ_{yy}) and converts to σ_1 and σ_2. The area for stress monitoring is 0.32 km^2 (8% of the total area, 4 km^2). In situ stresses (S_h, S_H) are indicated by a dot. The amount of principal stress changes ($\Delta\sigma_1$, $\Delta\sigma_1$) occurring in the intact reservoir (Fig. 23a) and the fractured reservoir (Fig. 23b) from the beginning to the final state (ca. 60 h) are (7 MPa, 8 MPa) and (10 MPa, 17 MPa), respectively. For

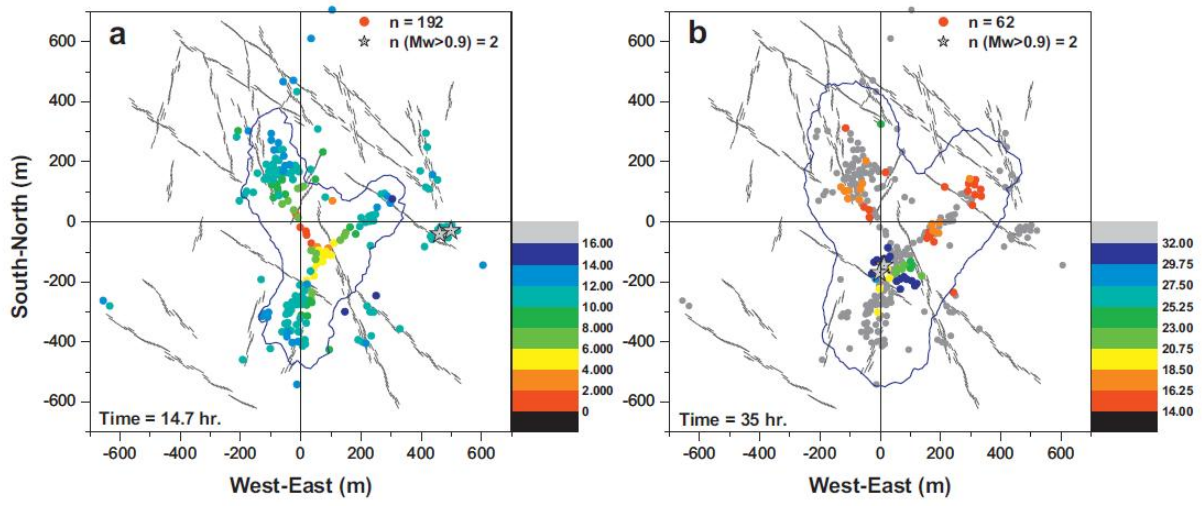

Figure 21. Spatio-temporal distributions of the induced seismic events in fractured reservoir during (a) pre-shut-in and (b) post-shut-in, resulting from cyclically increasing rates fluid injection. Color represents the occurrence time (in hour) of the induced events. In (b), pre-shut-in events are displayed in gray dots. Distribution of fluid pressures of 0.1 MPa and 70 MPa are indicated by blue and red contours, respectively. Time of the fluid pressure contours is indicated at the bottom left corner. Injection point is at model origin. Gray stars are the events with $M_w > 0.9$. (For interpretation of the references to color in this figure legend, the reader is referred to the web version of this article.)

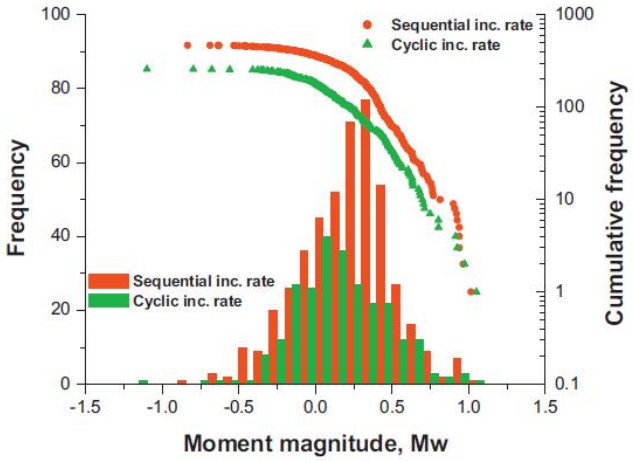

Figure 22. Histograms (left) of the moment magnitudes of the induced seismic events and their magnitude vs. cumulative frequency distribution (right) resulting from sequentially increasing rate of injection (red) and cyclically increasing rate of injection (green). (For interpretation of the references to color in this figure legend, the reader is referred to the web version of this article.)

clarity, pre-shut-in records are indicated by broken lines. Dashed lines in back represent iso-lines where the ratio σ_1/σ_2 remains same.

In the intact reservoir, the initial anisotropic stress state (at 0 h, σ_1/σ_2 = 1.28) is less deteriorated during the pre-shut-in period. The ratio σ_1/σ_2 becomes even higher (1.30) at the time of shut-in which leads to more anisotropic fracture propagation pattern during the post-shut-in period.

In the fractured reservoir, the principal stresses significantly change during the pre-shut-in period, whereas the amount of stress changes in the intact reservoir is minor. This is due to the pre-existing joints with low strength which can easily fail and slide during the repeated pressurizing-depressurizing. As a result, the ratio σ_1/σ_2 changes to 1.08 (at 20.67 h) from 1.27, which means that the stress state in the 0.32 km² area around the injection point became more isotropic. This is why the aspect ratio of the induced event cloud made during the stimulation is small (Fig. 13a). The ratio σ_1/σ_2 increases to 1.36 (at 21.53 h) during the last residual 5 MPa period which leads to two event clouds (clusters of blue events in Fig. 13a). The ratio σ_1/σ_2 then decays to 1.2 (at 58.3 h) which is less than the starting ratio (1.27). Less anisotropic stress state (σ_1/σ_2 = 1.2) resulted in two event clouds (red-orange events in Fig. 13b). However, their locations are left and right tips of the main cloud, although the far-field maximum in situ stress is still S_H = 75 MPa in NS. The reason for this might be that the stress state in the 0.32 km² area around the injection point has been severely changed during the pre-shut-in period and the local maximum principal stress direction has changed from NS to EW during the post-shut-in period.

The difference between the cyclic 5 MPa residual and 35 MPa residual scenarios is that the amount of pressure difference applied to the injection point is larger in case of cyclic 5 MPa residual injection. This represents a case where a material is subjected to high amplitude fatigue loading. After the reservoir is subjected to cyclic 5 MPa residual injection (analogous to high amplitude fatigue loading), the stress state at the injection point area becomes more anisotropic (Fig. 23a, where the σ_1/σ_2 changes from 1.28 to 1.3).

We interpret that the cyclic 5 MPa residual injection (high amplitude fatigue loading) has changed the stress state to a more favorable for anisotropic and long fracturing pattern. The cyclic 35 MPa residual injection represents, on the other hand, a case where a material is subjected to low amplitude fatigue loading, which is not strong enough to weaken the reservoir as much as it does in the cyclic 5 MPa residual injection. However, this trend (long and anisotropic fracturing after high amplitude fatigue injection) becomes obscure, when

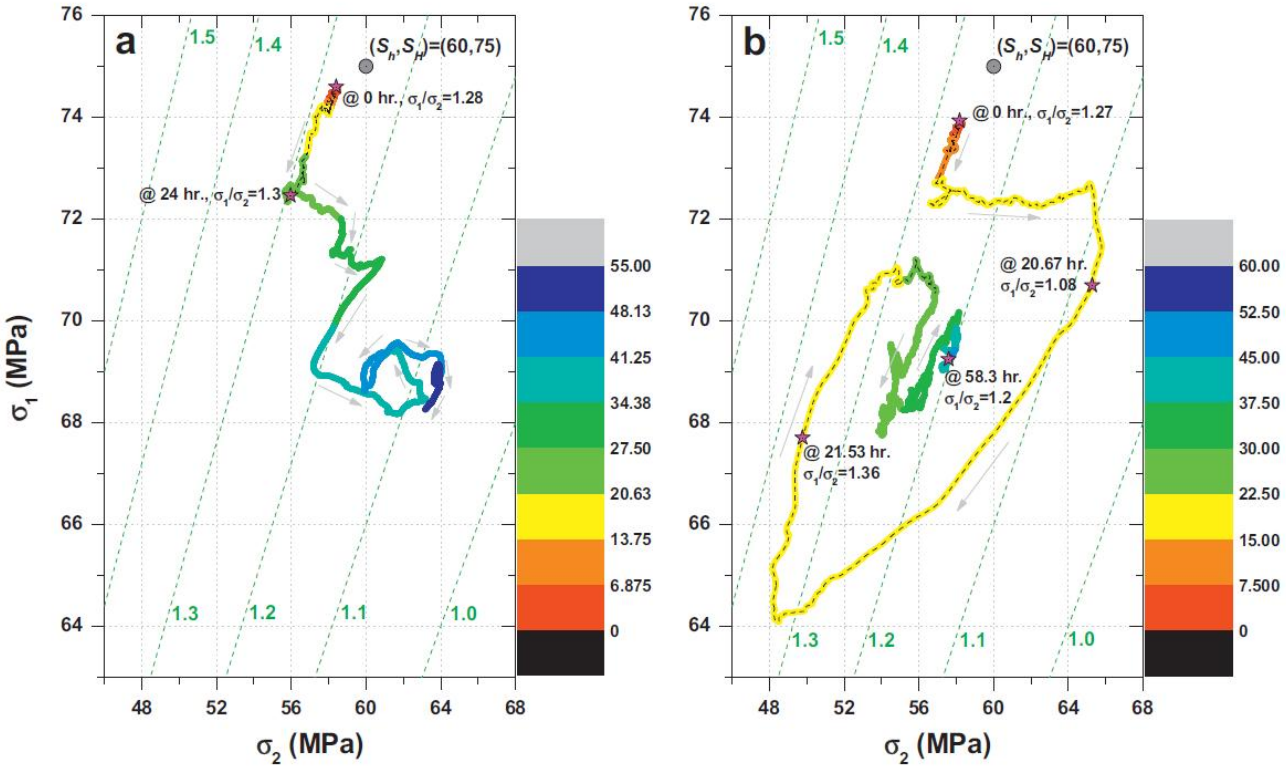

Figure 23. Temporal changes of maximum and minimum principal stresses (σ_1 vs. σ_2) from local stress monitoring approach (monitoring area: 0.32 km²) for (a) intact reservoir and (b) fractured reservoir stimulated with cyclic 5 MPa residual injection. In situ stresses (S_h, S_H) are indicated by a dot. Pre-shut-in records are indicated by broken line along the σ_1 vs. σ_2 trajectory.

Table 3
Summary of the overall shapes of the induced event clouds from ten fluid injection scenarios.

Reservoir type Injection scheme	Intact Pressure controlled	Fractured Pressure controlled	Fractured Flow rate controlled
Continuous type	Strong anisotropy Thin, Linear (Fig. 7a and b)	Strong anisotropy Broad, Areal (Fig. 12a and b)	Strong anisotropy Broad, Areal (Fig. 19a and b)
Cyclic type 5 MPa residual	Strong anisotropy Thin, Linear (Fig. 8a and b)	Weak anisotropy Broad, Areal (Fig. 13a and b)	X
Cyclic type 35 MPa residual	Weak anisotropy Thin, Linear (Fig. 9a and b)	Strong anisotropy Broad, Areal (Fig. 14a and b)	X
Pulse type	Isotropy Broad, Areal (Fig. 17a)	Isotropy Broad, Areal (Fig. 17b)	X
Cyclic type	X	X	Strong anisotropy Thin, Linear (Fig. 21a and b)

X: not modeled.

applied to the fractured model. This is due to the presence of joints which consume the input energy by frictional slipping. The fatigue pressurizing at the injection point somehow expands the reservoir volume and results in slip of the pre-existing joints, where the given energy is dissipated by the frictional sliding. The effect of high and low amplitude fatigue loading becomes less significant, not as much as it was when applied to the intact reservoirs.

In all fractured reservoirs, compared to the intact reservoirs (Figs. 7–9), large number of events is induced (far) ahead of the 0.1 MPa fluid pressure contour (fore front induced events, FFIE) (Figs. 12–15). Occurrence of such FFIE may not be well explained by the effective stress law where the Mohr circles are translated leftward with the amount equivalent to the increased fluid pressure. Such FFIE are induced because of the expanded volume of rock mass by fluid injection resulted in sliding and re-activation of the pre-existing joints even at far distance away from the injection point.

In case of pulse type injection, occurrence of the FFIE is more pronounced as the reservoir is subjected to rapid fluid injection, i.e. P_f reaches 250 MPa within 10 min, which serves similar to a dynamic loading. This is due to the elastic wave generated by the pulse pressurizing at the injection point that travels faster than the speed of fluid migration. More FFIE are observed in the fractured reservoir (Fig. 17b) compared to the intact reservoir (Fig. 17a).

Table 3 summarizes the overall shape of the induced event clouds resulting from ten injection scenarios on the intact and the fractured reservoirs simulated with the pressure controlled and flow rate controlled injections. In case of intact reservoir under pressure controlled injection, the shapes of the induced event clouds are all thin and linear. For the fractured reservoir, the shapes of the induced event clouds are broader and areal. When the fractured reservoir is simulated with flow rate controlled, the shapes of the induced event clouds are broad and areal. This is due to the fact that the fluid pressure is changing drastically during the stimulation, as the controlling factor is the flow rate and not the fluid pressure. Fractal dimensioning of the event clouds can provide more quantitative results.

For each scenario, we provided source mechanisms for the three largest magnitude induced events. Depending on the R value of the moment tensor for an event (Section 2.4), the source mechanism is classified into three types: tensile, shear and implosion. When $R > +30\%$ the event is tensile source, when $-30\% < R < +30\%$ the event is shear source, when $R < -30\%$ the event is implosion source. Seismic information of the three largest events is provided in Table 2, which include moment magnitude M_w, R value, source mechanisms and period (pre- or post-shut-in) when the event is induced. From seismological point of view, it is usually believed that a large magnitude event is double-couple (shear) source mechanism. However, our modeling showed that the large magnitude events induced by fluid injection do not always show double-couple character. This finding is in line with field observations made at several EGS sites, where many large magnitude induced events are with non-double-couple focal mechanisms, e.g. in the geothermal field of Larderello in Italy (*Console and Rosini*, 1998) and The Geysers geothermal area in California, USA (*Ross et al.*, 1996) and Carthage Cotton valley gas field in Texas, USA (*Sileny et al.*, 2009), to name a few.

Fracture propagation patterns in the fractured reservoir under flow rate controlled injection differ significantly (Figs. 19 and 21). Cyclic injection produced uni-directional fracture growth (during 0–4 h) followed by multi-directional fracture growth in three directions consequently resulting in "Y" shape with longer and thinner fracture propagation pattern. This is due to the repeated loading–unloading which allows more adaptation time to the reservoir to decide the optimized fracture propagation direction for the loading that follows after (*Zang et al.*, 2013). However, in case of sequentially increasing flow rate injection, the induced event cloud is more areal and broader. This is due to relatively short adaptation time to decide which direction is the optimum fracture growth path that minimizes the consumption of the input energy.

A similar observation for the size of the damaged zone was found in laboratory experiments (confined asymmetric triaxial compression testing) on granite under displacement rate and acoustic emission rate controlled loading (*Zang et al.*, 1998, 2000, 2002). Comparing the two rupture paths in deformed granite sample tested by (a) acoustic emission rate controlled (slow) loading and (b) displacement rate controlled (faster) loading, acoustic emission rate controlled loading produced clean and thinner fracture compared to the rupture path generated by the displacement rate controlled loading. In acoustic emission rate controlled loading, the fracture tip has more adaptation time to find the optimum propagation path, minimizing the consumption of input energy, resulting in narrower damaged zone.

It can be argued that our 2D model approach may not be appropriate as the induced seismicity in EGS is 4D problem (seismicity cloud evolving in 3D space with time). Moreover, the vertical in situ stress plays a significant role in reality, which is excluded in the 2D modeling. 3D modeling is needed

in this context and some advances are being made. However, objectives of this numerical study are to examine if the presented numerical method, though it is 2D, is capable of (i) reproducing typically observed induced seismicity phenomena in EGS, e.g. creation of new fractures, re-activation of the pre-existing joints, post-shut-in seismicity, post-shut-in large magnitude event, non-double-couple source events, Kaiser effect, moment magnitude vs. frequency distribution of the induced events following the Gutenberg-Richter law, etc. and (ii) providing insights for how one should design a stimulation treatment for a geothermal reservoir to mitigate the effects of induced seismicity and at the same time optimize the EGS for more efficient heat exchangers.

As the results are dependent on the particle arrangement and resolution (particle size), it is recommended to run a few more simulations with same model parameters and same initial/boundary conditions but with different particle arrangements. By doing this, more general results can be obtained. In PFC modeling, the particles are circular and rigid bodies with a finite mass. The assumption of particle circularity and rigidity are often argued as limitations of the method when the PFC is applied to simulate rock strength and damage under uniaxial and triaxial compression. Stress-strain curves of rock samples under uniaxial/triaxial compression often exhibit curvatures at early stage of loading, which is due to combination of closing of pre-existing cracks lying perpendicular to major principal stress and grain deformation itself (*Yoon*, 2007). Also, the ratio of compressive to tensile (direct or indirect) strength of the PFC rock model is far lower (4–5) than what is typically observed in laboratory rock testing of granite (10–20) (*Yoon*, 2007; *Yoon et al.*, 2011). The particle circularity and rigidity are the main cause of the discrepancy. There are numerous approaches tried to solve these issues, for example, by particle clumping (*Cho et al.*, 2007; *Yoon et al.*, 2011, 2012) and grain-based modeling (*Potyondy*, 2010). However, as these issues are problematic when the PFC modeling is applied to small scale rock deformation modeling, the assumption of particle circularity and rigidity remain reasonable when movements along interfaces account for most of the deformation in a material (*Potyondy and Cundall*, 2004), as it is in this study.

Last issue is whether poro-elastic and thermo-elastic effects are considered in this numerical modeling. A 3D modeling study by *Ghassemi and Zhou* (2011) which takes into account thermo-poro-elasticity showed that a fracture response to fluid injection/extraction in EGS is largely influenced by the poro-elastic effect in the early stage of injection, whereas thermo-elastic effect becomes dominant for large injection time. Many other studies have shown that thermal effect, i.e. cold water injection into hot rock, is significant on crack aperture opening and fracture slippage and potentially on reservoir seismicity (*Ghassemi et al.*, 2007, 2008; *Zhou and Ghassemi*, 2011).

In this numerical study, thermo-elastic/-plastic effects are not taken into account. Incorporating thermal effect on rock mass and fracture deformation and injection fluid rheology, e.g. density and viscosity change, etc. are issues of ongoing studies. In terms of poro-elastic effect, it can be argued that the presented modeling has poro-elasto-plasticity nature. The fluid pressure in the void spaces surrounded by the particles (Fig. 2) exerts forces on the particles. Therefore, the net stress acting at the particle contacts is reduced by the amount of fluid pressure contained at a void space. By doing this, the law of effective stress, hence poro-elastic effect, is incorporated but in in-direct way. As this modeling study aims at simulation of hydraulic stimulation where the poro-elastic effect should be dominant in the early stage of fluid injection (*Ghassemi and Zhou*, 2011), incapability of modeling thermo-elastic/-plastic effect would not have significant influence on the overall modeling results. However, as pointed out by *Ghassemi and Zhou* (2011) and *Ghassemi et al.* (2007, 2008), future modeling approaches should be aimed at incorporating thermo-elastic/-plastic effects to be applied to, in particular, long term EGS modeling (stimulation, circulation and extraction).

6. Conclusions

This numerical study investigated hydraulic fracturing of a synthetic geothermal reservoirs with granitic properties for intact rock and pre-existing joints and the resulting pattern of the induced event cloud using a hydro-mechanical coupled discrete particles joints model. By testing various types of fluid injection scenarios in intact and fractured reservoirs, following conclusions are drawn and a few suggestions are made for further research.

(1) Intact reservoir stimulated by cyclic fluid injection showed the largest extent of fracture propagation. Such repeated pressurizing-depressurizing at the injection point may play a significant role in optimizing an EGS when the reservoir is relatively intact or with low density and low persistent joints.
(2) Fractured reservoir stimulated by monotonic and cyclic increase of injection pressure showed occurrence of post-shut-in larger magnitude events and Kaiser effect which are typically observed phenomena in EGS. These results demonstrate that the presented numerical model well captures the induced seismicity related phenomena in EGS.
(3) For optimized stimulation of a naturally fractured reservoir, unlike in the intact reservoir, cycling the injection pressure may not be effective and the pressure difference between the maximum and minimum levels should be designed carefully. Also, speed and duration of the pressure relaxation between the cycles also play significant roles. Such behaviors could be explained by the fatigue loading in material science.
(4) Similarity of the numerical results to the field observations is achieved in case of flow rate controlled fluid injection. The results showed that soft stimulation technique, i.e. cyclic increase of flow rate with low injection rate maintained between the cycles, produces longer fracture propagated length with largest magnitude events confined within the pre-shut-in period. It is recommended to conduct a full parametric study on the injection parameters for cyclic injection, e.g. number of cycles, durations and rates of a single cycle, rate increment and interval time for the subsequent cycles, etc.
(5) Comparing the two flow rate controlled injection scenarios, it shows that the cyclic injection results in larger volume of injected fluid, less number of total events and larger magnitude events, slower relaxation of the fluid pressure after shut-in, longer and thinner propagated fractures. The results imply that the cyclic stimulation treatment shows potential in mitigating the effects of larger magnitude events. However, how much the reservoir permeability can be enhanced should be further investigated, and advances are being made regarding this issue.
(6) Pulse type fluid injection is simulated and showed isotropic fracture propagation pattern and significantly large magnitude events. This finding indicates that pulse type fluid injection may not be a good choice for a stimulation strategy for both intact and naturally fractured reservoirs.

Acknowledgements

The fluid flow algorithm used in this study is a modified form of the original which was provided by Dr. J. Hazzard

(Itasca) to whom authors are grateful. This work was supported by the European Union funded project GEISER (Geothermal Engineering Integrating Mitigation of Induced Seismicity in Reservoirs, FP7-ENERGY-2009-1, Grant No. 241321-2). In the course of the manuscript revision, the first author was financially supported by a project funded by German Federal Ministry for the Environment, Nature Conservation and Nuclear Safety (Grant No. 0325451C, Project name: Development of petrothermal reservoirs). In this respect, we would like to thank Prof. Ernst Huenges, Prof. David Bruhn and Prof. Günter Zimmermann (GFZ, Section 4.1 Reservoir Technologies). Comments from the two anonymous reviewers are acknowledged.

References

Al-Busaidi, A., Hazzard, J.F., Young, R.P., 2005. Distinct element modeling of hydraulically fractured Lac du Bonnet granite. Journal of Geophysical Research 110, B06302.

Baisch, S., Vörös, R., Rothert, E., Stang, H., Jung, R., Schellschmidt, R., 2010. A numerical model for fluid injection induced seismicity at Soultz-sous-Forêts. International Journal of Rock Mechanics Mining Sciences 47, 405–413.

Baria, R., Baumgärtner, J., Gérard, A., Jung, R., Garnish, J., 1999. European HDR research programme at Soultz-sous-Forêts (France) 1987–1996. Geothermics 28, 655–669.

Cho, N., Martin, C.D., Sego, D.C., 2007. A clumped particle model for rock. International Journal of Rock Mechanics and Mining Sciences 44, 997–1000.

Console, R., Rosini, R., 1998. Non-double-couple microearthquakes in the geothermal field of Larderello, central Italy. Tectonophysics 289, 203–220.

Cornet, F.H., Bérard, Th., Bourouis, S., 2007. How close to failure is a granitic rock mass at a 5 km depth? International Journal of Rock Mechanics Mining Sciences 44, 47–66.

Cuenot, N., Dorbath, C., Dorbath, L., 2008. Analysis of the microseismicity induced by fluid injections at the EGS Site of Soultz-sous-Forêts (Alsace, France): implications for the characterization of the geothermal reservoir properties. Pure and Applied Geophysics 165, 797–828.

Evans, K.F., Kohl, T., Rybach, L., Final Report – July 1998. European Hot Dry Rock Geothermal Energy Research Programme 1996–1998: Project No. JOR3-CT95-0054 1998. Analysis of the hydraulic behaviour of the 3.5 km deep reservoir during the 1995-1997 test series, and other contributions to the European Hot Dry Rock Project Soultz-sous-Forêts, France.

Feignier, B., Young, R.P., 1992. Moment tensor inversion of induced microseismic events: evidence of non-shear failures in the $-4 < M < -2$ moment magnitude range. Geophysical Research Letters 19 (14), 1503–1510.

Gentier, S., Rachez, X., Tran Ngoc, T.D., Peter-Borie, M., Souque, C., 2010. 3D Modelling of the medium-term circulation test performed in the deep geothermal site of Soultz-sous-Forêts (France). In: Proceedings of World Geothermal Congress 2010, Bali, Indonesia, 25–29 April 2010.

Ghassemi, A., Tarasovs, S., Cheng, A.H.-D., 2007. A three-dimensional study of the effects of thermo-mechanical loads on fracture slip in enhanced geothermal reservoir. International Journal of Rock Mechanics and Mining Sciences 44, 1132–1140.

Ghassemi, A., Nygren, A., Cheng, A.D.-H., 2008. Effects of heat extraction on fracture aperture: a poro-thermoelastic analysis. Geothermics 37 (5), 525–539.

Ghassemi, A., Zhou, X., 2011. A three-dimensional thermo-poroelastic model for fracture response to injection/extraction in Enhanced Geothermal Systems. Geothermics 40, 39–49.

Gutenberg, B., Richter, C.F., 1956. Earthquake magnitude, intensity, energy and acceleration (second paper). Bulletin of the Seismological Society of America 46, 105–145.

Hazzard, J.F., Young, R.P., 2002. Moment tensors and micromechanical models. Tectonophysics 356, 181–197.

Hazzard, J.F., Young, R.P., 2004. Dynamic modeling of induced seismicity. International Journal of Rock Mechanics Mining Sciences 41, 1365–1370.

Hazzard, J.F., Young, R.P., Oates, S.J., 2002. Numerical modeling of seismicity induced by fluid injection in a fractured reservoir. In: Proceedings of the 5th North American Rock Mechanics Symposium, Mining and Tunnel Innovation and Opportunity, Toronto, Canada, 7–10 July 2002, pp. 1023–1030.

Hökmark, H., Lönnqvist, M., Fälth, B., Technical Report TR-10-23 2010. THM-issues in repository rock – thermal, mechanical, thermo-mechanical and hydro-mechanical evolution of the rock at the Forsmark and Laxemar sites. SKB – Swedish Nuclear Fuel and Waste Management Co., pp. 26–27.

Itasca Consulting Group Inc., 2008. PFC2D – Particle Flow Code in 2 Dimensions, Version 4.0, Minneapolis.

Itasca Consulting Group Inc., 2012. Technical Memorandum – 5.0 Parallel Bond Enhancement.

Kraft, T., Mai, P.M., Wiemer, S., Deichmann, N., Ripperger, J., Kästli, P., Bachmann, C., Fäh, D., Wössner, J., Giardini, D., 2009. Enhanced Geothermal Systems: mitigating risk in urban areas. EOS 90 (August (32)).

Kulatilake, P.H.S.W., Malama, B., Wang, J., 2001. Physical and particle flow modeling of jointed rock block behavior under uniaxial loading. International Journal of Rock Mechanics Mining Sciences 38, 641–657.

Labuz, J.F., Zang, A., 2012. ISRM suggested methods Mohr–Coulomb failure criterion. Rock Mechanics and Rock Engineering 45, 975–979.

Madariaga, R., 1976. Dynamics of an expanding circular fault. Bulletin of the Seismological Society of America 66, 639–666.

Majer, E.L., Baria, R., Stark, M., Oates, S., Bommer, J., Smith, B., Asanuma, H., 2007. Induced seismicity associated with Enhanced Geothermal Systems. Geothermics 36, 185–222.

Marone, C., 1998. Laboratory-derived friction laws and their application to seismic faulting. Annual Review of Earth and Planetary Sciences 26, 643–696.

Mas Ivars, D., Potyondy, D.O., Pierce, M., Cundall, P.A., 2008. The smooth-joint contact model. In: Proceedings of 8th World Congress on Computational Mechanics (WCCM8) and 5th European Congress on Computational Methods in Applied Sciences and Engineering (ECCOMAS 2008), Venice, Italy, 30 June–4 July 2008, Paper A2735.

Mars Ivars, D., (Doctoral Thesis) 2010. Bonded particle model for jointed rock mass. Department of Land and Water Resources Engineering, Royal Institute of Technology (KTH), Stockholm, Sweden.

McClure, M., Horne, R., 2013. Is pure shear stimulation always the mechanism of stimulation in EGS? In: Proceedings of Thirty-Eighth Workshop on Geothermal Reservoir Engineering, Stanford University, Stanford, CA, 11–13 February 2013, SGP-TR-198.

Michelet, S., Toksöz, N., 2005. Characterizing the Mechanics of Fracturing from Earthquake Source Parameter and Multiplet Analysis: Application to the Soultz-sous-Forêts Hot Dry Rock Site. Massachusetts Institute of Technology, Earth Resource Laboratory, available at http://hdl.handle.net/1721.1/67880

Mukuhira, Y., Asanuma, H., Niitsuma, H., Häring, M.O., 2013. Characteristics of large-magnitude microseismic events recorded during and after stimulation of a geothermal reservoir at Basel, Switzerland. Geothermics 45, 1–17.

Park, E.-S., Martin, C.D., Christiansson, R., 2004. Simulation of the mechanical behavior of discontinuous rock masses using a bonded-particle model. In: Proceedings of 6th North American Rock Mechanics Symposium, Rock Mechanics Across Borders and Disciplines, Houston, TX, 5–10 June 2004, Paper ARMA 04-480.

Potyondy, D.O., Cundall, P.A., 2004. A bonded-particle model for rock. International Journal of Rock Mechanics Mining Sciences 41, 1329–1330.

Potyondy, D.O., 2010. A grain-based model for rock: approaching the true microstructure. In: Proceedings of Rock Mechanics in the Nordic Countries 2010 (Bergmekanikk i Norden 2010), Kongsberg, Norway, 9–12 June 2010.

Ross, A., Foulger, G.R., Julian, B.R., 1996. Non-double-couple earthquake mechanisms at The Geysers geothermal area, California. Geophysical Research Letters 23 (8), 877–880.

Rummel, F., Baumgartner, J., 1991. Hydraulic fracturing stress measurements in the GPK-1 borehole, Soultz-sous-Forêts. Geothermal Science and Technology 3, 119–148.

Scholz, C., 1990. The Mechanics of Earthquakes and Faulting. Cambridge University Press, Cambridge, UK, 439 pp.

Shimizu, H., Murata, S., Ishida, T., 2011. The distinct element analysis for hydraulic fracturing in hard rock considering fluid viscosity and particle size distribution. International Journal of Rock Mechanics

Mining Sciences 48, 712–727.
Sileny, J., Hill, D.P., Eisner, L., Cornet, F.H., 2009. Non-double-couple mechanisms of microearthquakes induced by hydraulic fracturing. Journal of Geophysical Research 114, B08307.
Valley, B., Evans, K.F., 2006. 2006. Strength and elastic properties of the Soultz granite. In: EHDRA Scientific Conference, 15–16 June 2006.
Yoon, J., 2007. Application of experimental design and optimization to PFC model calibration in uniaxial compression simulation. International Journal of Rock Mechanics and Mining Sciences 44, 871–889.
Yoon, J., Jeon, S.,2009. Use of a modified particle-based method in simulating blast-induced rock fracture. In: Proceedings of the 9th International Symposium on Rock Fragmentation by Blasting – FRAGBLAST9. Granada, Spain, 13–17 September 2009, pp. 371–380.
Yoon, J.S., Jeon, S., Zang, A., Stephansson, O., 2011. Bonded particle model simulation of laboratory rock tests for granite using particle clumping and contact unbonding. In: Proceedings of the 2nd International FLAC/DEM Symposium, Continuum and Distinct Element Numerical Modeling in Geomechanics, Melbourne, Australia, 14–16 February 2011, Paper 08-05.
Yoon, J.S., Zang, A., Stephansson, O., 2012. Simulating fracture and friction of Aue granite under confined asymmetric compressive test using clumped particle model. International Journal of Rock Mechanics Mining Sciences 49, 68–83.
Yoon, J.S., Zang, A., Stephansson, O., 2013. Hydro-mechanical coupled discrete element modeling of geothermal reservoir stimulation and induced seismicity. In: Proceedings of Thirty-Eighth Workshop on Geothermal Reservoir Engineering, Stanford University, Stanford, CA, 11–13 February 2013, SGP-TR-198.
Zang, A., Wagner, F.C., Stanchits, S., Dresen, G., Andresen, R., Haidekker, M.A., 1998. Source analysis of acoustic emissions in Aue granite cores under symmetric and asymmetric compressive loads. Geophysical Journal International 135, 1113–1120.
Zang, A., Wagner, F.C., Stanchits, S., Janssen, C., Dresen, G., 2000. Fracture process zone in granite. Journal of Geophysical Research 105 (B10), 23651–23660.
Zang, A., Stanchits, S., Dresen, G., 2002. Acoustic emission controlled triaxial rock fracture and friction tests. In: Dyskin, A.V., Hu, X., Sahouryeh, E. (Eds.), Structural Integrity and Fracture. Lisse, Swets & Zeitlinger, pp. 289–294.
Zang, A., Stephansson, O., 2010. Stress Field of the Earth's Crust. Springer Sci-ence + Business Media B.V., Dordrecht, 143 pp.
Zang, A., Yoon, J.S., Stephansson, O., Heidbach, O., 2013. Fatigue hydraulic fracturing by cyclic reservoir treatment enhances permeability and reduces induced seismicity. Geophysical Journal International 195, 1282–1290.
Zhao, X., Young, R.P., 2011. Numerical modeling of seismicity induced by fluid injection in naturally fractured reservoirs. Geophysics 76 (6), WC167–WC170.
Zhou, X., Ghassemi, A., 2011. Three-dimensional poroelastic analysis of a pressurized natural fracture. International Journal of Rock Mechanics and Mining Sciences 48 (4), 527–534.